

Chapter 16: Micro-Optical Techniques

Kartik Srinivasan¹, Matthew T. Rakher¹, and Marcelo Davanço^{1,2}

¹*Center for Nanoscale Science and Technology, National Institute of Standards and Technology*

Gaithersburg, MD 20899-6203; e-mail: kartik.srinivasan@nist.gov

²*Maryland NanoCenter, University of Maryland, College Park, Maryland 20742, USA*

Chapter 16: Micro-Optical Techniques	1
16.1 Introduction.....	2
16.2 Anatomy of a micro-photoluminescence (micro-PL) setup.....	6
16.2.1 Excitation source.....	11
16.2.2 Optics for focusing the excitation beam onto the sample.....	17
16.2.3 Optics for PL collection.....	24
16.2.4 Emission detection.....	28
16.2.5 Imaging	41
16.3 Measurements using a micro-PL setup.....	49
16.3.1 Microcavity lasers.....	49
16.3.2 Quantum dot spectroscopy.....	53
16.4 Related micro-optical techniques.....	59
16.4.1 Photoluminescence excitation (PLE) spectroscopy.....	60
16.4.2 Electroluminescence	62
16.4.3 Angle-resolved reflectivity	64

16.5.1 Beam alignment	69
16.5.2 Beam profiling	71
Acknowledgements.....	72
References.....	72

16.1 Introduction

This chapter focuses on optical measurements in which spatial resolution on the order of the wavelength of light provides meaningful, distinct information from that which can be obtained through bulk measurements, such as those described in Chapter 6. These techniques include photoluminescence spectroscopy, photoluminescence excitation spectroscopy, electroluminescence, and angle-resolved reflectivity measurements. There are several physical systems for which the ability to perform such measurements with wavelength-scale spatial resolution is needed. For example, it is essential when interrogating nanofabricated photonic devices (Figure 1(a)) such as microcavity lasers (McCall 1992), where the optical cavities are a few micrometers in each planar dimension and are fabricated in arrays with a device-to-device spacing of tens of micrometers. Here, the spatial resolution is needed to distinguish between cavities and between a cavity and unprocessed regions of the chip. A second example is an ensemble of solid-state emitters in or on a substrate (Figure 1(b)), which encompasses structures such as epitaxially grown self-assembled quantum dots (Michler 2003) embedded in a semiconductor material, colloidal quantum dots in solution or deposited on a substrate (Alivisatos 1996, Murray 1993), fluorescent molecules in a host matrix (Moerner 1999), and impurity color centers in a crystal (Gruber 1997). These materials may exhibit a density gradient

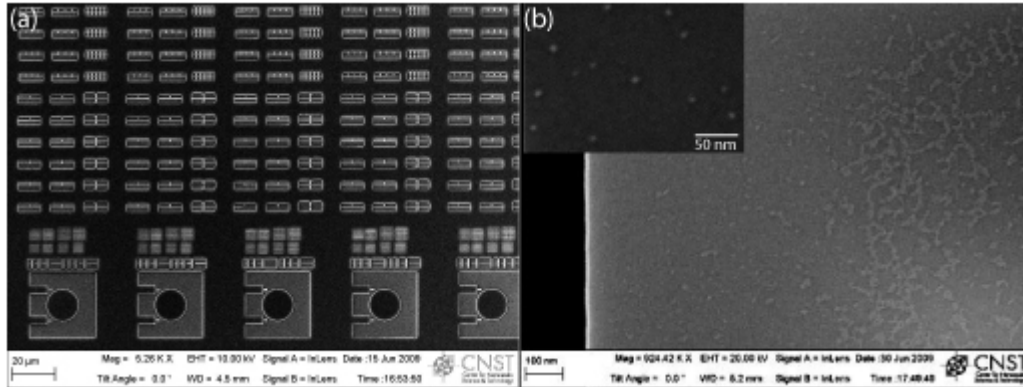


Figure 1: (a) Scanning electron microscope (SEM) image of a two-dimensional array of nanophotonic devices (waveguides, hole arrays, and microdisk cavities) to be interrogated through micro-PL measurements. The minimum required spatial resolution is that needed to go from device to device on the chip. (b) SEM images of PbS quantum dots (QDs) spun on a Si substrate. With sufficient spatial resolution, micro-PL can be used to study QD ensembles of varying density. The inset shows the number of QDs present within a $\approx 260 \text{ nm} \times 170 \text{ nm}$ field across the sample, so that spatially-resolved measurements can provide an understanding of optical properties as a function of the number of excited emitters, ultimately reaching the single emitter limit in very dilute (≈ 1 emitter per μm^2) regions. Our discussion is restricted to techniques that achieve diffraction-limited spatial resolution through “conventional” methods of high numerical aperture, free space far-field optics. For the near-infrared wavelengths that are our interest, this produces a length scale on the order of a micrometer (hence the title “Micro-optical techniques”). This chapter does not cover some of the important developments in the quest for obtaining better spatial resolution, including near-field scanning optical microscopy (NSOM), the topic of Chapter 17 and so-called superresolution techniques like stimulated emission depletion microscopy (Hell 2009) (Chapter 15). Such tools can provide a wealth of added information, such as spatial profiles of microcavity modes (Balistreri 1999), or the ability to distinguish between single fluorescent centers within a dense array (Betzig 1993). Nevertheless, as we shall see throughout this chapter, wavelength-scale spatial resolution is in many cases preferred, since the improved resolution of a technique like NSOM comes at the cost of increased complexity and sacrifice in collection efficiency. Space constraints also prevent us

from addressing promising recent developments in improving photoluminescence collection efficiencies, particularly for embedded media like quantum wells or quantum dots, through solid immersion lenses (Gerardot 2007) or external waveguide probes (Srinivasan 2007).

While this chapter has the general title of “Micro-optical techniques,” its primary focus is micro-photoluminescence (micro-PL). As discussed in Chapter 6, photoluminescence (PL) can be loosely defined as a process in which a material absorbs light at one wavelength and emits light at another (usually red-shifted) wavelength. For our purposes, micro-PL is a measurement in which the pump beam has been focused down to a micrometer-scale spot on the sample, and the emission from a portion of this region is collected and spectrally resolved. There are several reasons why we have chosen micro-PL as our representative micro-optical technique. The first is that it is one of the most widespread methods of device characterization, providing information about the electronic structure of the material and electronic transitions between its states. Next, the experimental apparatus needed for conducting micro-PL measurements is sufficiently general so that photoluminescence excitation, electroluminescence, and angle-resolved reflectivity measurements can be incorporated into the same setup if relatively straightforward additions are made. The setup required for micro-Raman spectroscopy (Delhaye 1975), a complementary technique that can provide information about low frequency transitions within the material (such as vibrational and rotational modes), is conceptually similar, though the specific pieces of equipment needed may differ. Finally, as we use micro-PL routinely within our own laboratory, we have the opportunity to share considerations we made when constructing our setup.

Our goal is to provide the reader with the essential information needed to construct and use a micro-PL setup. The content of this chapter lies somewhere between a set of instructions for a senior undergraduate laboratory and a formal review of research results, and is biased

heavily towards the former. The reader should be aware that micro-PL and related optical techniques such as confocal fluorescence microscopy have been used within various research fields for many years, and providing an adequate history of the technique and the scientists who pioneered it would be a significant undertaking that is beyond the scope of what we hope to accomplish. References that may provide the reader with valuable insight include standard optics texts (Hecht 1998), books on optical spectroscopy (Demtroder 1998), Hobbs's book on practical construction of electro-optic systems (Hobbs 2000), and Novotny and Hecht's recent book on nano-optics (Novotny 2006). Several major optics vendors also include "principles of operation" notes in their catalogs, which can be invaluable when determining which optics to purchase. There are also several other review articles on micro-PL, a few of which we cite here (Kasai 1995, Gustafsson 1998, Moerner 2003).

The organization of this chapter is as follows. In Section 16.2, we present a detailed description of a typical micro-PL setup and the process by which it is designed. We have partitioned the apparatus into different sub-systems, and for each sub-system, we discuss design choices and tradeoffs involved. In Section 16.3, we present examples of data acquired from a micro-PL setup, describe what the measurements tell us about the system, and what further information could be obtained through additional measurements. In Section 16.4, we describe extensions to micro-PL setups that allow for new information to be unlocked. These include photoluminescence excitation spectroscopy, where the excitation wavelength is tuned to provide some insight into the electronic structure of the system; electroluminescence measurements, where the excitation channel is electrical rather than optical, and angle-resolved reflectivity, where the resonant optical response of a system can be probed. Finally, in Section 16.5, we include a couple of general lab procedures and rules of thumb that can help beginners when

building a new micro-optical measurement setup.

16.2 Anatomy of a micro-photoluminescence (micro-PL) setup

The core idea of a micro-PL setup is to focus an excitation source down to a wavelength-scale spot on a sample, where it is absorbed and generates emission (typically at a different wavelength) that is directed into a detector such as a grating spectrometer, through which an emission spectrum can be produced. Spatial resolution is obtained through the limited extent of the pump and collection areas, and PL maps can be generated through translation of the sample and/or excitation beam. If the sample to be interrogated contains specific features to which the pump beam must be aligned, imaging using a white light source and an appropriate camera may be required. The remainder of this section is devoted to providing a detailed, practical description of how these functionalities can be achieved. As is the case whenever one builds optical setups, appropriate attention to safety must be paid, and the user should consult with his/her laser safety officer to ensure compliance with laser safety standards.

A schematic of a typical micro-PL apparatus is shown in Figure 2, where a single objective is used to focus the pump beam on the sample and to collimate emission from the sample. For convenience, we have partitioned this setup into several sub-systems: (1) Excitation source, (2) Optics for focusing the excitation beam onto the sample (pumping), (3) Optics for PL collection (collection), (4) Detection, (5) Imaging, and (6) Sample environment/positioning. Obviously, this separation is not absolute, and various optical components may serve dual roles, for example, in both sample excitation and collection. Before we proceed to spend time outlining the components of each sub-system, it is worthwhile to first outline a few general considerations that must go into the design of such a measurement apparatus.

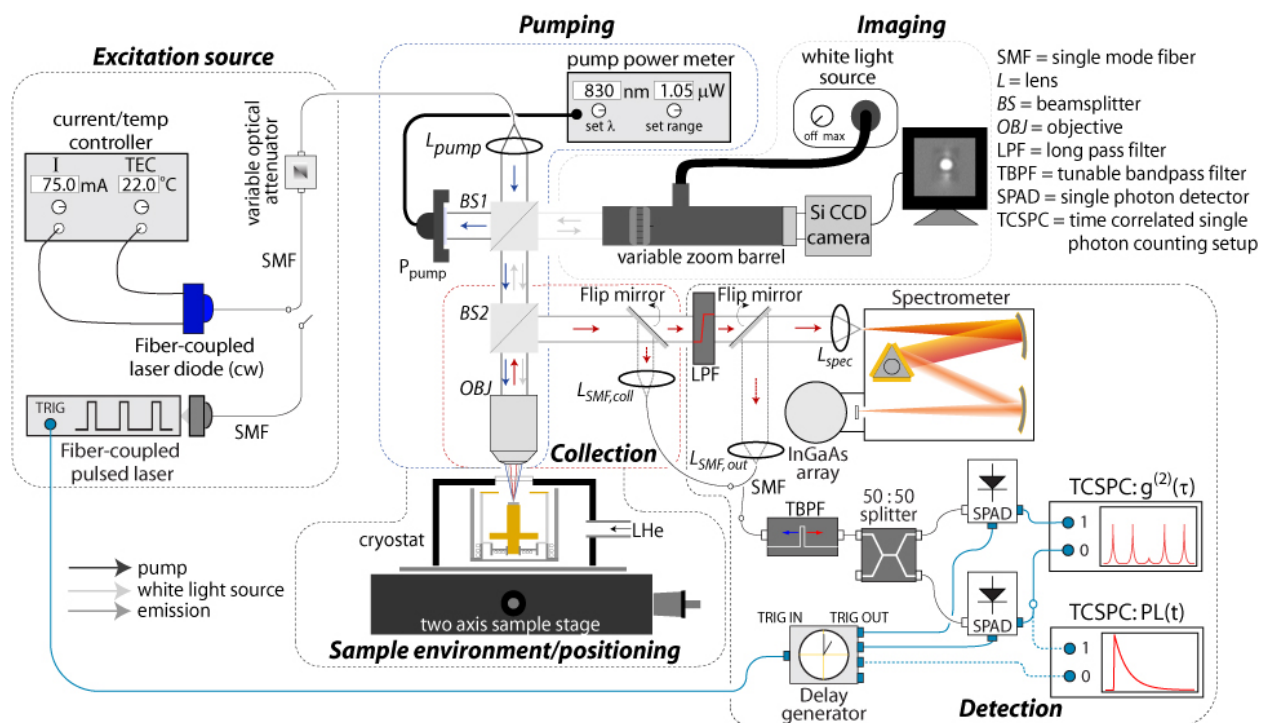


Figure 2: Schematic of a typical micro-PL setup for investigating a sample in a cryogenic environment. SMF= single mode fiber, BS=beamsplitter, L=lens, OBJ= objective, LPF = long pass filter, TBPF=tunable bandpass filter, SPAD=single photon avalanche photodiode, TCSPC=time-correlated single photon counting.

These general considerations largely involve some knowledge of the specific physical system(s) to be characterized. Knowledge of the wavelength-dependent absorption and emission cross-sections determines the required properties of the excitation source and detector. The required information here can sometimes be quite approximate, and in some cases obtained from literature or from ensemble absorption and/or macro-PL measurements of the system. For example, in a micro-PL measurement of semiconductor quantum dots, the bandgap energy of the host semiconductor will determine the appropriate wavelength for photogeneration of carriers, while the likely emission band determines whether a Si-based or InGaAs-based detector should be used. Optics such as beamsplitters, lenses, and objectives are often anti-reflection coated for use over specific wavelength ranges. If certain optics are to be used in multiple roles (e.g., pump beam focusing, emission collection, and white light imaging), chromatic aberration can be an

important factor in deciding what type of optical element to choose. Depending on the characteristics of the material under investigation, control of the polarization of the excitation beam and collected signal can be important, and will have to be taken into account in the choice of optics. The environment in which the sample is to be characterized (e.g., ambient vs. low temperature) can impose a minimum separation between the sample surface and focusing/collection optics, setting limits on the excitation/collection spot and the fraction of emission that will be collected. It can also determine whether pumping and collection will be done on the same side of the sample, or whether backside excitation/collection can be employed. Regardless of the specific implementation, keeping the optical paths as short as possible is generally advisable. Finally, and perhaps most importantly, the user will impose constraints on the setup based upon what is required from the measurement, and the budget available. An experiment requiring limited spectral resolution and moderate collection efficiency from an ensemble of visible wavelength emitters will necessitate a setup that is an order of magnitude less complex (and expensive) than the one needed to produce spectrally resolved time-dependent PL dynamics from single near-infrared emitters. The objectives of the experiment thus set the priority level given to different parts of the setup.

One might envision planning a micro-PL setup by going through the following process:

1) Determine the general architecture of the setup. What are the most critical aspects of the setup? Will pumping and collection be done from the same side, on opposite sides, or in a non-collinear fashion? How will imaging (if needed) be integrated? The goal of this step is to have a general layout in place for the excitation, collection, and imaging paths. This layout, along with the expected excitation and collection wavelengths, will go a long way towards determining what type of optics (aspheres, achromatic doublets, microscope objectives, etc.) to use; 2) Based on

the system to be investigated and the type of measurement needed, select an excitation source; 3) Specify the minimum allowable working distance (separation between the sample and the optic's front surface) for the optic that will be focusing light onto the sample. Next, specify the required excitation spot size and determine the optics needed to achieve this; 4) Specify the required collection angle, and if applicable, collection area. Determine if this is compatible with the minimum working distance allowed by the setup, and with the already specified pump focusing optics, if any optics will be shared. If necessary, consider how additional optics can be added to limit the collection area. If portions of the excitation and collection beam paths are to be shared, decide on what optics will be used to combine/separate them; (5) Specify if the collected signal is to be spectrally resolved and if so, the required spectral resolution. Decide on what type of detector is going to be used to measure the collected and spectrally resolved light, and any optics that might be needed to couple into it; (6) Specify the requirements for sample imaging (resolution, field of view, zoom range), and determine the appropriate optics and camera/video system to meet these needs and to integrate the white light beam path with the existing pump/collection optics; 7) Decide whether translation of the sample or translation of the optics is the preferred approach for performing micro-PL measurements across the sample; and 8) Double check steps 1-7 and iterate as needed.

As a concrete example, let us review the thought process used to construct our micro-PL setup (Figure 2) for studying near-infrared InAs quantum dots. 1) Along with low-temperature capabilities, our specific experiments require a system in which additional probes (electrical, near-field optical) can be incorporated. These capabilities are not relevant to this chapter except that they influence the design of the system – in particular, incorporation of such probes is most easily accomplished through front side pumping and collection. Furthermore, we need to image

our samples with micrometer-scale spatial resolution, and this also has to be done through the front side. Our priority is collection efficiency, followed by imaging capability and pump efficiency, though there is a minimum requirement for all three; 2) We use a 830 nm laser diode for excitation, as it can efficiently excite the quantum dot states through absorption in the GaAs and wetting layers that surround the quantum dots; 3) The minimum working distance is set by the separation between our cryostat top window and the sample surface, and is ≈ 15 mm (relatively large due to the introduction of electrical/optical probes), precluding the use of almost any commercially available fluorescence microscope. We require a pump spot size of $\approx 2 \mu\text{m}$, though the collection spot is more important than the pump spot in our measurements. Optics that can achieve this include large diameter aspheres and long working distance microscope objectives; 4) We want to collect 1300 nm emission from an area of $\approx 2 \mu\text{m}^2$, though there is some flexibility here depending on the exact characteristics of the sample to be studied. While these requirements are in principle compatible with both large diameter aspheres and long working distance microscope objectives, we choose the latter due to better chromatic aberration properties (also needed for the white light imaging). Cube beamsplitters or dichroic mirrors will be used to combine/separate the pump and collection beam paths; 5) The primary detector will be a grating spectrometer equipped with a cooled InGaAs array. Long pass edge filters will remove the residual pump signal, and the collimated collected signal will need to be focused into the spectrometer. For time-resolved measurements, we will use InGaAs photodiodes and single photon counters with single mode fiber inputs, requiring a convenient method to switch between detectors. Furthermore, the photodiodes and single photon counters will require separate optics to focus the collected signal into the single mode fiber. 6) Sample imaging with approximately 1 μm resolution is needed since we will be aligning the pump beam to microfabricated devices.

Adjustable zoom is needed in situations where near-field probing is combined with micro-PL. These requirements are compatible with an infinity-corrected long working distance microscope objective and zoom barrel system. 7) Though small adjustments of the pump beam position on the sample provide fine translation capabilities, sample translation is preferred since it requires little re-alignment of optics, and high resolution stepping is not required in our measurements.

With the above in mind, we now delve into each of the micro-PL subsystems in detail.

16.2.1 Excitation source

16.2.1.1 Continuous wave sources

We begin by considering continuous wave (cw) excitation sources for use in steady-state PL spectroscopy. The most obvious requirement is that the source be of the appropriate wavelength. For example, consider common III-V semiconductor materials like GaAs and InP, which often serve as a host for light-emitting structures like quantum wells and quantum dots (Chapter 2), and have their room temperature band gaps at approximately 870 nm and 930 nm, respectively. By photoexciting GaAs or InP-based light-emitting structures at photon energies above the band gap, significant absorption of optical energy and production of carriers within the GaAs/InP layers can be achieved. Upon relaxation (e.g., due to phonons), these carriers can then fill the appropriate states of the quantum wells/dots, eventually resulting in recombination and emission. Spectrally-resolved photoluminescence spectra, such as those discussed in Section 16.4, will display not only the emission due to the quantum wells/dots, but can also show emission from recombination at the GaAs band-edge and at defect centers in the material.

An inexpensive and compact excitation source for micro-PL measurements on these III-V systems is a semiconductor diode laser (Coldren 1995) emitting at 780 nm or 830 nm. Such lasers, typically edge-emitting Fabry-Perot or distributed feedback structures, can be driven by a

current source and stabilized by a temperature controller that regulates the current to a thermoelectric cooler that is often integrated with the laser diode. Threshold currents are typically in the 100 mA range, with output powers of tens or even hundreds of mW available. If wavelengths other than 780 nm or 830 nm are required, semiconductor laser diodes based on the technologically mature GaAs, GaP, and InGaAsP systems provide coverage over the \approx 630 nm to 1600 nm range, while III-nitride semiconductors can cover green and blue wavelengths. Other choices for visible wavelength excitation include HeNe, Ar ion, and frequency doubled Nd:YAG lasers, as discussed in Chapter 6. The choice of laser is dictated by issues including power, spectral linewidth, form factor, beam shape, and cost.

A typical edge-emitting diode laser supports emission from multiple cavity modes, and thus does not provide spectrally narrow excitation. In many instances, this is of no concern, and indeed, even an incoherent light emitting diode can be used as an excitation source if enough output power is available. When spectrally narrow emission is needed, distributed feedback or fiber Bragg grating stabilized lasers, in which a grating is used to select a specific mode of the device, are an option. Diffraction gratings can also be incorporated into external cavity designs, such as the Littrow and Littman-Metcalf geometries (Paschotta 2008). Here, the laser diode has a high reflectivity (HR) coating on one facet and is antireflection-coated on the other facet. The cavity is formed between the HR facet and the grating (Littrow configuration) or between the HR facet and a grating that is followed by an external mirror (Littman-Metcalf). By rotating either the grating (Littrow) or mirror (Littman-Metcalf), the laser wavelength is tuned over the diode's gain bandwidth, and the external cavity geometry typically provides a narrower linewidth (on the order of 1 MHz) than a standard laser diode. As a result, such external cavity diode lasers (ECDLs) can be used in photoluminescence excitation (PLE) experiments, as discussed in

Section 16.3, although the available tuning range (usually a couple tens of nm for wavelengths less than 1 μm and as much as 100 nm for wavelengths near 1.55 μm) may be too narrow, requiring more widely tunable solid-state lasers.

One of the most commonly used tunable solid-state lasers is the Ti:sapphire laser (Paschotta 2008), an optically pumped (in the green) laser that typically provides wavelength coverage between ≈ 700 nm to 900 nm, though broader wavelength coverage is possible depending on the power requirement and optics used. The laser can also be used as a pump source in different wavelength conversion units, such as an optical parametric oscillator (used to generate longer wavelengths) or a frequency doubler (used to generate shorter wavelengths) (Chapter 7). These features, along with output power levels that can significantly exceed those of tunable diode lasers, make cw Ti:sapphire lasers a versatile source for micro-PL and micro-PL spectroscopy experiments. Disadvantages include high cost (typically several times more expensive than an ECDL), large size (along with the pump laser, can occupy a significant portion of an optical table), and support equipment (often requiring water cooling and significant electrical power consumption). Finally, we note that a host of other cw tunable laser sources have been used in PL experiments, including tunable dye lasers (wavelength coverage in the 550 nm to 780 nm range) and color center lasers (various emission bands in the 800 nm to 3 μm region). The development of bright and compact supercontinuum sources (Chapter 7) has made them a potential (quasi-cw) PL spectroscopy source, in which different bandpass filters can be used to select for specific excitation wavelengths.

16.2.1.2 Pulsed sources

The need for pulsed excitation can arise in a few different situations. While investigation of time-dependent phenomena is the most common (Chapter 12), other instances include steady-

state spectroscopy of structures in which thermal dissipation is a problem (e.g., nanofabricated membrane structures, such as the photonic crystal microcavity lasers to be discussed in Section 16.3.1) and material systems in which photobleaching, photodarkening, or blinking occur (Moerner 2003). In such situations, the parameters of the pulsed excitation may be chosen to limit heating or improve signal-to-noise/background levels. Pulsed excitation is also used in lock-in measurements, which can improve the signal-to-noise ratio (SNR) by shifting the detection frequency away from DC. On the other hand, steady-state spectroscopy of thermally stable and photostable structures using pulsed excitation (without lock-in detection) causes a decrease in the number of collected photons, by a fraction approximately equal to the duty cycle (contingent upon the emission lifetime).

The time-dependent measurements considered in this chapter are the PL decay and second order correlation function, which are commonly performed measurements for single solid state emitters (ultrafast pump-probe spectroscopy and related techniques are the focus of other chapters within the book in section III). For these measurements, the key characteristics of the laser source are its wavelength, repetition rate, pulse width, and energy. In general, a PL lifetime measurement is not a single-shot experiment, but rather the average over many experiments in which the sample is excited by a pulse and its PL intensity is detected over a range of times that are delayed with respect to the pulse (Chapter 12). The period (inverse of the repetition rate) must therefore be sufficiently long so that all of the important dynamics occur in the interval between pulses. The pulse width must be narrow enough to occupy a small fraction of the PL decay. The pulse energy is set according to the physics of the system under investigation (e.g., to generate a specific average number of electron-hole pairs per pulse in a III-V quantum dot).

For convenience, we consider two types of pulsed sources, those which are created by

modulating an existing cw source, and those based on mode-locking. One straightforward and direct way to modulate a cw source is through the energy source that pumps the laser. For example, a semiconductor laser diode can be modulated by switching its current between above threshold and below threshold, creating an 'on' and an 'off' state, with the pulse width given by the length of time over which the current is kept above threshold (this is called gain switching). Such current modulation of semiconductor lasers is complicated by carrier dependent gain dynamics (Coldren 1995, Yariv 2007), influencing the achievable pulse shapes and widths and ultimately necessitating the use of external electro-optic modulators in certain applications. For situations in which gain-switched diode laser pulses are acceptable, they can be generated through the current driver for the laser, which will often have a radio frequency (RF) input that can be driven by a general purpose waveform generator. In this scenario, typical maximum modulation speeds are on the order of 1 MHz, limited by the current source electronics. For generation of pulse widths on the order of 100 ps, dedicated drivers and laser diodes are commercially available. These systems produce moderate output powers (a few mW of average power), and are a compact and significantly less expensive option than most of the mode-locked lasers to be discussed below. Furthermore, the repetition frequency is often controllable, and can be set to a fraction of its maximum value. This can be important when using the source across systems in which carrier dynamics exhibit very different timescales.

Another option is to use an external modulator, which is a gate that blocks the output laser for a desired period of time and at a desired rate. An inexpensive external modulation method is found in a mechanical chopper, which is often used with a lock-in amplifier or as a simple way to reduce heating. The chopper is essentially a very stable rotating fan, with the pulse repetition rate and width being determined by its speed and blade widths (typical rates are

in the range of one Hz to a few kHz; tens of kHz are possible in some units). To achieve faster repetition rates and narrower pulse widths, acousto-optic modulators (AOMs) or electro-optic modulators (EOMs) can be used (Yariv 2007), providing modulation bandwidths on the order of 100 MHz (AOM) or 10 GHz (EOM). At the fastest modulation speeds, the primary cost involved in an EOM is not in the modulator itself, but rather in the modulator driver, which must produce high speed electrical pulses. Other than cost, one of the principal challenges in using EOMs for lifetime measurements is in the achievable on/off ratio (the extinction ratio), and its stability over time. Achieving the highest levels of extinction and stability requires precise control of the polarization state of light going into the modulator. Control of the environment (temperature) and feedback on a DC bias applied to the modulator may also be necessary.

Mode-locked lasers constitute a second class of pulsed laser sources for time-dependent PL measurements, with the Ti:sapphire laser being one of the most common choices (Chapter 7). As discussed earlier, cw Ti:sapphire lasers offer the combination of high output powers and broad wavelength tuning ranges. Generation of short pulses is done through mode locking, where the relative phases of the laser cavity's multiple modes are fixed (through introduction of an intracavity saturable absorber or through intracavity loss/phase modulation), resulting in a pulse train (Diels 2006, Chapter 7). Mode-locked Ti:sapphire lasers routinely produce sub-100 fs pulse widths at a rate of 80 MHz, which is set by the round-trip time of light in the cavity. Importantly, this repetition rate sets the timescale over which dynamics can be measured – to use an 80 MHz Ti:sapphire laser to study a system with a PL lifetime > 10 ns, some form of pulse selection (a 'pulse picker') must be used for downsampling. Finally, other tunable sources previously described, such as dye, color center, and rare-earth-doped glass lasers, can also be mode-locked. Rare-earth doped optical fibers, of crucial importance to optical communications,

have also been mode-locked to produce near-single-cycle optical pulses (4.3 fs in Krauss 2009), and their small form factors and relative stability make them attractive alternatives in situations where the accessible wavelength range and power levels are appropriate.

16.2.2 Optics for focusing the excitation beam onto the sample

This section is devoted to describing how the excitation beam, whose extent is usually a few mm, is focused down to a micrometer-scale spot on the sample surface. We discuss shaping to produce a clean Gaussian beam, and focusing of the beam to a desired pump spot size.

16.2.2.1 Beam shaping

Although certain situations might call for the use of an elliptical or doughnut-shaped beam, in most situations, the desired input into a micro-PL setup is a circular Gaussian beam, which will eventually be collimated to fill the clear aperture of the focusing lens (discussed in more detail in Section 16.2.2.2). The amount of shaping needed depends on the laser source. Lasers based on Fabry-Perot cavities may naturally produce a Gaussian-shaped beam, while edge-emitting semiconductor lasers can produce an elliptical, diverging beam. In other circumstances, the laser output may have a waist significantly larger or smaller than desired. Since semiconductor diode lasers are such an inexpensive and compact option for micro-PL measurements, we will discuss how to circularize their output.

When circularizing an elliptical beam, the first step is to determine its beam shape through beam profiling (Section 16.5.2), or from information provided by the laser diode manufacturer. Two common methods to shape the beam employ either cylindrical lenses or anamorphic prism pairs. A cylindrical lens affects light along only one axis, so that two orthogonal cylindrical lenses, chosen with a focal length ratio equal to the ratio of the beam divergence angles along the axes of the elliptical beam, will produce a collimated circular beam.

An anamorphic prism pair also magnifies a beam along only one axis. The prism pair is placed in the beam path after the laser output has been collimated. The angles of the two prisms relative to the beam propagation direction determine the level of magnification, with ratios of two to six being common. An adjustable prism pair allows for circularization of beams of differing eccentricities, while a fixed prism pair can be housed in a compact mount that is usually significantly smaller than the footprint required for a pair of cylindrical lenses, although it should be noted that the input and output beams from the prism pair are not collinear.

Light from the excitation source might also require spatial filtering, in which the goal is to remove unwanted spatial fluctuations. One method of spatial filtering is through a pinhole aperture mounted on a multi-axis translation stage. The basic idea is to focus the laser beam into a pinhole, which is small enough to block high spatial frequency noise components (whose radial distance from the propagation axis is proportional to the spatial frequency), but large enough to transmit the majority of the laser beam power propagating in the spatial mode of interest; a pinhole diameter 1.5 times the expected Gaussian beam diameter is a common choice. The cleaned-up beam can then be re-collimated and introduced into the rest of the micro-PL setup.

An alternate method for spatial filtering is to couple the laser into a single mode optical fiber. The fiber acts as a modal filter, allowing only its fundamental mode to propagate a significant distance, and the output beam launched from a single mode fiber closely approximates a Gaussian beam. One note of warning when fiber coupling the laser output is that back reflections from the fiber can be a destabilizing influence on the laser, and are particularly problematic in some cases. A common method to reduce back reflections is to use a fiber that has been terminated in an angled physical contact (APC) connector, where the fiber end face has been polished at an 8° angle. The highest levels of protection from back reflected light are

usually accomplished by a Faraday isolator, a non-reciprocal optical element that can produce isolation levels routinely in excess of 30 dB. Many lasers offer an isolator output as an option.

A potential disadvantage of the single mode fiber approach is that even with relatively good alignment, the coupling efficiency might only be 50 %, and depending on the setup stability, it may need to be periodically adjusted. An advantage of the method is that these small misalignments only affect the efficiency with which the output Gaussian beam is launched, and not the spatial profile of the beam. In our laboratory, we generally use fiber-coupled semiconductor diode lasers as PL excitation sources. Along with the spatial filtering aspects described above, coupling light into a single mode fiber allows the laser to be separated by a significant distance from the rest of the setup, as light propagates through single mode fibers with very low loss (<1 dB/km), though if polarization preservation is important, special considerations must be made (e.g., use of polarization maintaining fiber). This is of practical convenience when building the setup, and also makes it convenient to switch between sources by simply disconnecting one fiber and connecting a second (followed by an adjustment of the collimation optics if the excitation wavelength is significantly different). In addition, many vendors offer fiber-pigtailed semiconductor lasers, where the laser-to-fiber coupling has been completed and the system has been packaged so that the alignment remains fixed in place. These sources offer power levels at the mW to tens of mW level, though higher power lasers are available, for example, at 980 nm (the pump band for erbium-doped fiber amplifiers).

16.2.2.2 Beam focusing

This step involves taking the Gaussian beam produced by the excitation source, and collimating it to an appropriate diameter so that the subsequent focusing optic will produce the desired spot size on the sample surface. Figure 3(a) schematically depicts the block of the

overall micro-PL setup (Figure 2) devoted to these tasks, while Figures 3(b)-(e) are schematics of individual beam shaping operations that may be employed.

There are several options for the beam focusing optic, including microscope objectives, aspheres, and doublets. Singlet lenses are also a possibility, though spherical and chromatic aberration errors usually suggest that one of the aforementioned optics is a better choice. Otherwise, the decision between doublet, asphere, and microscope objective often comes down to the specifics of the experimental layout. If the focusing optic is to be used exclusively with the excitation source, a simple doublet or asphere can work quite well. If the optic is to be used for both excitation and collection, the difference in wavelengths can lead to chromatic aberrations, so that achromatic doublets, achromatic microscope objectives, or low dispersion aspheres are better options. An achromatic doublet consists of a pair of lenses, made of different materials, so that two different wavelengths can be brought into focus in the same plane, providing a level of chromatic correction not available in most single element optics. If the optic is to be used for white light imaging along with excitation and collection, an apochromatic microscope objective (element *OBJ* in Figure 3) is a versatile option that provides significant levels of spherical and chromatic aberration correction. The price of such optics essentially monotonically increases with the complexity and aberration-correcting ability – apochromatic objectives are multi-element, multi-material systems that can significantly outperform achromatic doublets and aspheres but whose cost can exceed them by an order of magnitude.

Along with spot size and chromatic considerations, other factors in choosing an optic include its working distance, depth of focus or confocal parameter (the distance along the propagation axis over which the beam area changes by a factor of two), and clear aperture (which determines how large an input beam can be accommodated). The working distance is

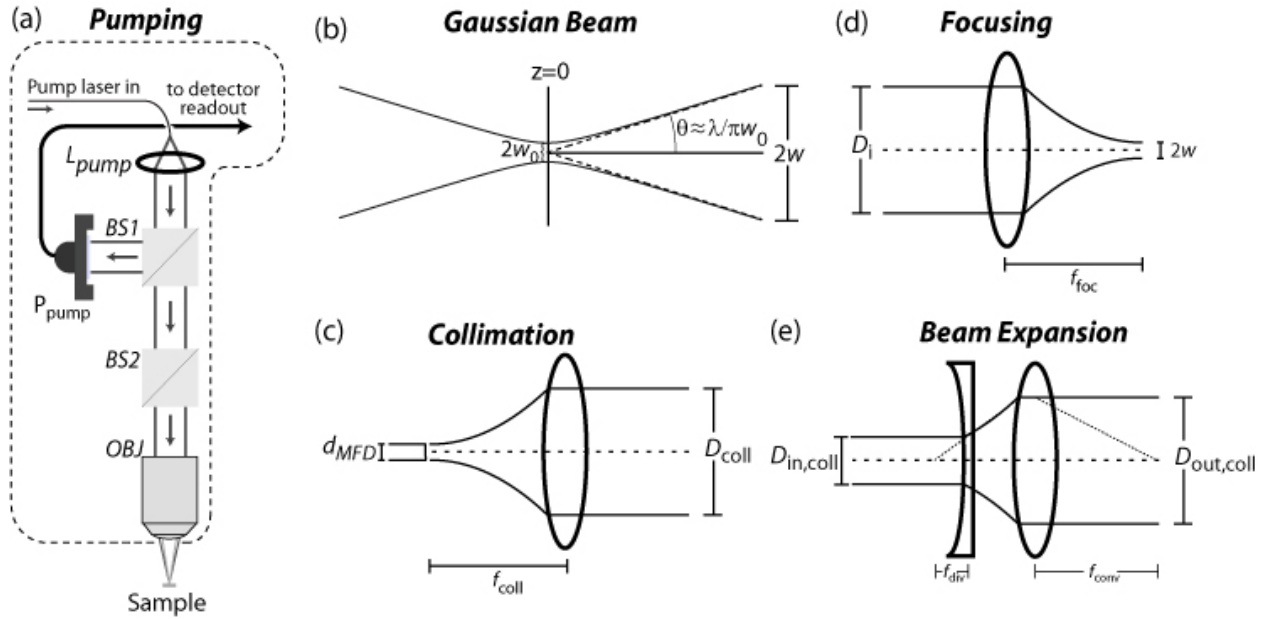


Figure 3: (a) Pumping section of a micro-PL setup, taken from Figure 2. (b) Gaussian beam schematic, showing the beam waist and divergence angle. (c) Optics for pump collimation from a single mode fiber, (d) focusing, and (e) beam expansion. In (e), $D_{out,coll}/D_{in,coll} \approx f_{conv}/f_{div}$. The lens shown is meant to be generic and could be an achromatic doublet, aspherical lens, or microscope objective. $BS1$ and $BS2$ are beamsplitters used to combine/separate the collection and white light imaging beam paths (not shown).

important if the sample to be interrogated must be cooled in a cryostat, or simultaneously electrically or optically contacted with external probes, as in both cases there is a minimum separation that can be achieved between the optic and the sample. In contrast, fluorescence experiments on molecules spun onto a glass slide often place the optic within 1 mm of the sample. As working distance generally decreases with shorter focal lengths and higher resolving powers, there is usually a tradeoff to be made between working distance and smallest possible spot size.

As the beam produced by many laser sources can be reasonably approximated as Gaussian, formulas from Gaussian beam optics (Yariv 2007, Siegman 1986) can be used to estimate parameters such as the focused pump spot size. Let us recall some of the important points of Gaussian beam optics, referring to Figure 3(b). The electric field transverse to the propagation direction ($E(r)$) has the form

$$E(r) = E_0 e^{-r^2/w^2(z)}, \quad (1)$$

where E_0 is the initial value of the field, r is the distance from the center of the beam, and $w(z)$ is the radial distance from beam center (at propagation distance z) for which $E=E_0/e$. The beam attains a minimum radius w_0 , called the beam waist, at a specific location in the propagation direction ($z=0$ here), and expands quadratically as a function of z as given by the formula:

$$w(z) = w_0 \sqrt{1 + \left(\frac{z}{z_R}\right)^2} \quad (2)$$

The parameter z_R is called the Rayleigh range and is given by $z_R = \pi w_0^2/\lambda$, so that $w = 2w_0$ at $z = \pm z_R$, with $2z_R$ being called the confocal parameter or the depth of focus. For $|z| \gg z_R$, the beam essentially diffracts linearly, at an angle $\theta = \lambda/\pi w_0$ with respect to the propagation axis.

Let us next consider how to collimate a Gaussian beam, taking as an example the beam exiting a single mode optical fiber (Fig. 3(c)). We assume a Gaussian beam with a diameter $2w_0 = d_{MFD}$, where d_{MFD} is the fiber's mode field diameter.¹ Assuming we place the optic a focal length (f_{coll}) away from the fiber output, and $f_{coll} \gg z_R$, we determine the collimated beam diameter D_{coll} by equating the previously defined diffraction angle θ with $D_{coll}/2f_{coll}$, the expected diffraction angle due to geometric optics in the small angle limit (and equal to the optic's numerical aperture, as we shall discuss later). Doing so yields:

$$D_{coll} = \left(\frac{4\lambda}{\pi}\right) \left(\frac{f_{coll}}{d_{MFD}}\right) \quad (3)$$

As a concrete example, single mode optical fiber designed for 780 nm laser light has $d_{MFD}=5.6$ μm , so that an $f_{coll}=15$ mm asphere would produce $D_{coll}=2.7$ mm.

Now that the beam is collimated, it can be focused down by an optic with focal length f_{foc} ,

¹ The mode field diameter describes the extent of the beam propagating through the optical fiber, and rather than the physical fiber core diameter, is the appropriate parameter to use in calculations involving single mode fibers. Note that the mode field diameter varies as a function of wavelength.

as schematically depicted in Fig. 4(d). The formula to use is the same as the above (Eq. (4)), but we now calculate the output beam waist given an input collimated beam, that is

$$2w = \left(\frac{4\lambda}{\pi}\right) \left(\frac{f_{\text{foc}}}{D_{\text{coll}}}\right) \quad (4)$$

Combining these equations, we relate the focused spot size to the initial beam waist as:

$$2w = \left(\frac{f_{\text{foc}}}{f_{\text{col}}}\right) d_{\text{MFD}} \quad (5)$$

Thus, the minimum achievable spot size is given by the product of the ratio of the focal lengths of the two lenses and the mode field diameter of the initial beam. In our example from above, to achieve a spot size $2w = 1 \mu\text{m}$, we need $f_{\text{col}}/f_{\text{foc}} \approx 1/5$. In practice, the ability to achieve this (or even smaller spot sizes) can be practically limited by typical focal lengths for the optics, and by the constraint of the minimum working distance needed for the focusing optic. In addition, the collimated beam diameter produced by the first lens must fit within the clear aperture of the focusing lens. Continuing with our example, one might use an $f_{\text{col}} \approx 25 \text{ mm}$ lens to produce a $\approx 4.5 \text{ mm}$ collimated beam, which is then focused down by a $f_{\text{foc}} = 4.5 \text{ mm}$ lens with a clear aperture of 5 mm and working distance of 2.9 mm to a spot diameter of $\approx 1 \mu\text{m}$. If a larger working distance is needed, one option is a large diameter asphere, which can have a much longer focal length and working distance ($>10 \text{ mm}$), but also requires a large input beam. A second option is to use a long working distance objective, which combines sub-micrometer resolution capabilities with a working distance of about 20 mm and requires an input beam diameter of about 8 mm .

Equation 4 tells us that the achievable spot size is inversely proportional to the input collimated beam diameter. While we have assumed that this input beam has been generated by a single optic, it might not be practically possible to use a single element to generate a sufficient diameter to take advantage of the full power of the focusing optic. To do so, one can use

multiple lenses to expand the input beam and more completely fill the focusing optic. Such an expander (Figure 3(e)) consists of a pair of lenses, with the laser beam first expanded by a diverging lens (negative focal length) and then collimated by a converging lens (positive focal length). The diverging lens should be chosen to have a clear aperture sufficient to handle the incoming beam (which we have assumed is collimated), and the absolute value of the ratio of the converging lens focal length to the diverging lens focal length should equal the desired beam expansion factor. It is sometimes convenient to adjust the beam expansion ratio. Many optics vendors offer variable beam expanders, where additional lenses have been incorporated in the tube so that the effective focal length of the diverging or converging section of the expander can be varied through path length adjustment, allowing for differing levels of beam expansion.

As a final comment, it is usually important to know the pump power at the sample surface, so that, along with the pump spot area, the delivered pump intensity can be obtained. This intensity is important when comparing a PL spectrum to those produced by another setup. In Figure 3(a), a detector (P_{pump}) is placed at an open port of beamsplitter *BS1*, and by comparing the value measured here with a measurement taken at the sample location, we determine the multiplicative factor to apply to additional pump power measurements (in which the detector remains next to *BS1*). It is important to periodically re-check this factor, and to ensure that the chosen detector is compatible with the pump size at the point at which it is measured.

16.2.3 Optics for PL collection

In this section, we consider the optics needed to collect emission from the sample, schematically depicted in Figure 4(a). As discussed previously, selection of the optic is strongly influenced by how many roles it has to play in excitation, collection, and white light imaging. That being said, there are still some general comments that can be made. The first is that the

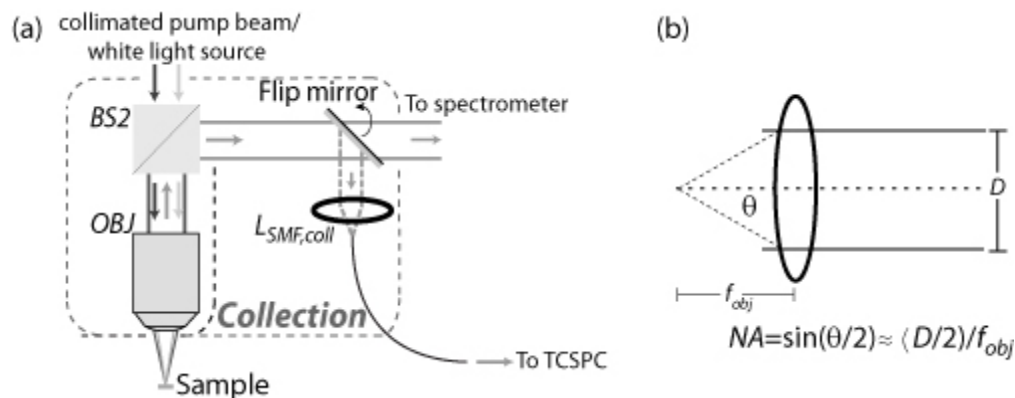


Figure 4: (a) Collection block of a micro-PL setup, re-displayed from Figure 3. (b) Numerical aperture of a converging lens.

numerical aperture (NA) of the optic, which is a measure of its acceptance angle (Figure 4(b)), plays a dominant role along with the working distance, which accounts for space constraints in the setup. A high NA optic collects light from a significant range of angles, and is therefore preferable from a light gathering perspective, but is often accompanied by a limited working distance. For example, a microscope objective with $NA=0.6$ (collection angle $\approx 60^\circ$) has a working distance less than 1 mm, while $NA=0.4$ (collection angle $\approx 40^\circ$) has a working distance of ≈ 3 mm to 4 mm. Aspheres can produce somewhat larger working distances (≈ 1.8 mm for $NA=0.68$), and large diameter (≈ 25 mm) aspheres that have recently been offered by many companies can combine $NA\approx 0.5$ with a working distance of around 10 mm.

Long working distance, apochromatic microscope objectives (element OBJ in Figure 4(a)) combine the high NA and working distance of large diameter aspheres with chromatic aberration correction. Typical specifications are $NA=0.42$ for a working distance of 20 mm and $NA=0.55$ for a working distance of 13 mm. Furthermore, unlike traditional microscope objectives, most long working distance apochromats are infinity corrected, meaning that they transform incoming light rays from the focus into a set of parallel rays that can later be focused to an image plane by a separate tube lens. The importance here is that the region between the objective and tube lens (the tube lens is a zoom barrel in Figure 2) is one in which additional

optics can be inserted without modification to the objective's working distance. For example, one might consider placing a rotatable polarizer in this section, if polarized emission measurements are needed.

At first glance, it would appear that the sample area over which emission is collected is equal to the pumped area, given by the focused excitation spot size discussed in Section 16.2.2, and indeed this is often the case. There are important exceptions, however. Carrier diffusion in semiconductors can generate an effective pumped area that is larger than the excitation spot. Early experiments in single quantum dot spectroscopy relied on fabrication methods to physically reduce the sample size from which emission could be collected, through etching of sub-micrometer width mesas or the use of sub-micrometer apertures in a deposited metal film.

The area over which emission is collected can also be limited through optics that aperture the collimated signal out of the microscope objective, thereby improving the spatial resolution. . A standard way to do this in confocal microscopy is to focus the beam through a pinhole before going into the detector (Chapter 15). A second option, which we employ, is to focus the light into a single mode optical fiber (element $L_{SMF, coll}$ in Figure 4(a)), which serves the same function. We calculate the ratio of the spot diameter collected by the fiber (D_{fiber}) to the spot diameter collected by the objective (D_{tot}) as follows. D_{tot} is approximately given by geometric optics as $D_{tot} = 2NA_{obj}f_{obj}$, where NA_{obj} and f_{obj} are the numerical aperture and focal length of the initial collection optic. Equation (4) then gives us the expression for D_{fiber} , so that in total, we have:

$$\left(\frac{D_{fiber}}{D_{tot}}\right) \approx \frac{\left(\frac{4\lambda}{\pi}\right)\left(\frac{f_{fiber}}{d_{MFD}}\right)}{2NA_{obj}f_{obj}} \quad (6)$$

where f_{fiber} is the focal length of the lens used to collect light into the single mode fiber. This ratio is also equal to $(2w_{fiber}/2w_{pump})$, the fraction of the pump spot diameter from which light is

being collected. Using equation (4) to re-write the pump spot diameter $2w_{pump}$ in terms of f_{obj} and D_i (the input excitation beam diameter), we have:

$$2w_{fiber} \approx 2w_{pump} \left(\frac{D_{fiber}}{D_{tot}} \right) \approx \frac{\left(\frac{4\lambda}{\pi} \right)^2 \left(\frac{f_{fiber}}{d_{MFD}} \right)}{2NA_{obj}D_i} \quad (7)$$

As a concrete example, our experiments involve collection at $\lambda=1.3 \mu\text{m}$ into a single mode fiber with $d_{MFD} = 7 \mu\text{m}$, using a long working distance apochromatic objective for which $NA_{obj} = 0.4$ and $f_{obj} = 10 \text{ mm}$. If our excitation source collimation optics produce $D_i = 7 \text{ mm}$, we should expect $2w_{pump} \approx 2.4 \mu\text{m}$. Let us now assume we want $2w_{fiber}$ to be reduced with respect to $2w_{pump}$, bearing in mind the limit (Δr) to which one can expect to resolve point emitters, as determined by diffraction, and given by (Novotny 2006) (Chapter 15):

$$\Delta r \approx 0.61 \frac{\lambda}{NA} \quad (8)$$

For our choice of objective and wavelength, one might try and achieve $2w_{fiber}=1.6 \mu\text{m}$. Equation (7) tells us that a $f_{fiber}=23 \text{ mm}$ coupling lens is an appropriate choice. While this reduction in collection area relative to pump area can come at the cost of collected photons for certain materials, for isolated single solid-state emitters like self-assembled quantum dots, the emission should be emanating from much smaller regions, so that the improved spatial resolution has come with no sacrifice in terms of collection efficiency.

Finally, we briefly consider options for combining the pump and collection paths in situations where the experiment calls for it. For example, in Figures 3(a) and 4(a), elements *BS1* and *BS2* depict cube beamsplitters used for this purpose. A non-polarizing cube beamsplitter can provide a 50:50 coupling ratio, with a clear aperture that is usually more than 75 % of the cube's edge length. Potential drawbacks are that the splitting ratio varies somewhat with wavelength (a pellicle beamsplitter provides better chromatic performance), and the specified wavelength range

may not cover both the pump and collection beams. In such cases, it is usually advantageous to choose a beamsplitter optimized for the collection wavelength, provided that sufficient pump power is available, and the transmission at the pump wavelength is measured so that the pump power delivered to the sample surface is known. Regardless, one disadvantage of the cube beamsplitter is in losing half the collected signal. To overcome this, a dichroic beamsplitter is a good option. A long wave pass (short wave pass) dichroic transmits the longer (shorter) wavelength and reflects the shorter (longer) wavelength. Since the dichroic reflectivity ($\approx 99\%$) typically exceeds its transmission ($\approx 90\%$), when collection efficiency is at a premium, it is advantageous to make it the reflected signal and use a short wave pass dichroic for red-shifted emission. On the other hand, collecting in transmission through a long wave pass dichroic can offer a broader bandwidth. Drawbacks in comparison to a cube beamsplitter are that it is not as broadband, and its properties are polarization dependent.

16.2.4 Emission detection

There are a tremendous number of options for detecting the PL signal, and our treatment here is just a small sampling of what can be done. We have divided this section into three pieces, the first detailing options for spectrally resolving the PL signal, the second describing the detectors that can be used to detect this spectrally-resolved emission to construct a PL spectrum, and the third describing time-dependent measurements that might be done.

16.2.4.1 Spectrally resolving the collected emission

The amount of spectral resolution needed obviously depends on the system under investigation and the specific measurement in question. In some cases, it is adequate to simply remove any residual pump beam, and detect emission over all other wavelengths (within the detector bandwidth). This can be done with a long wave pass interference filter, or if the pump

beam is sufficiently spectrally narrow, with a pump rejection filter. If the emission wavelength of interest is well-known, a bandpass filter can be used to provide better isolation between the collected signal of interest and background emission (depending on the isolation levels offered, the bandpass filter may be used in combination with an edge-pass filter). A tunable bandpass filter can be used to produce an emission spectrum if the signal past the filter is monitored as a function of filter position. A simple method for creating a tunable bandpass filter is to angle-tune a fixed bandpass filter, which usually is specified to operate at normal incidence. By adjusting the filter angle with respect to the incident beam, the center of the bandpass is shifted to shorter wavelengths. The exact design of the interference filter (e.g., number of cavities within the dielectric stack) will affect the steepness of the bandpass, which in turn will determine the available spectral resolution. A high resolution filter can be produced by a Fabry-Perot cavity (Siegman 1986), which is an optical resonator consisting of a pair of high reflectivity mirrors. These devices are specified in terms of the free spectral range (FSR), the wavelength separation between modes of the cavity (which show up as transmission peaks in the Fabry-Perot spectrum), and the finesse, the ratio of the free spectral range to the bandwidth of the modes. A scanning Fabry-Perot cavity allows for spectrally resolved measurements because the separation between mirrors can be varied through application of a voltage to a piezoelectric transducer on which one of the mirrors is mounted, thus changing the spectral position of the modes. For spectrally-resolved measurements, the criterion needed to use a scanning Fabry-Perot cavity is that the emission window must be narrower than the FSR, and the spectral resolution will be given by the bandwidth of the modes (determined by the reflectivity of the Fabry-Perot mirrors). Scanning Fabry-Perot cavities typically provide much better spectral resolution than either a tunable bandpass interference filter or a grating spectrometer, with picometer level resolution

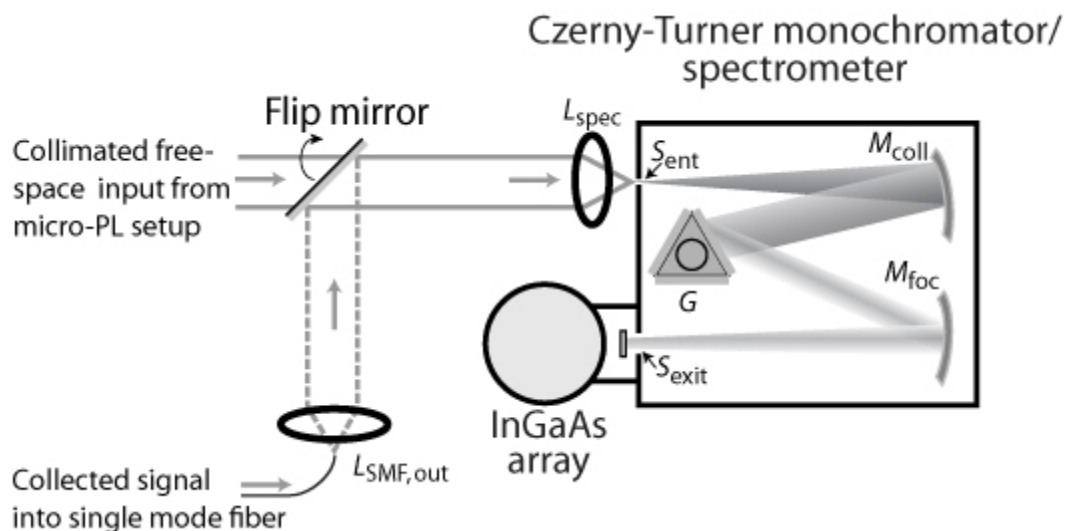


Figure 5: Diagram of a Czerny-Turner monochromator, equipped with an InGaAs array detector to produce a grating spectrometer, and with two input paths (collimated free-space beam and single mode fiber). Wavelength tuning is achieved through rotation of the grating G , with the grating turret holding three different gratings to allow for broad wavelength coverage by switching the gratings.

possible over spectrally narrow windows (e.g., FSR= 1 nm and finesse = 1000).

Diffraction gratings are another tool used to provide spectral resolution, as they take an input collimated beam and disperse it, causing a spatial separation of different wavelength components which then allows for wavelength-resolved detection. A commonly used instrument featuring a diffraction grating is a Czerny-Turner monochromator (Hobbs 2000), shown in Figure 5. The Czerny-Turner starts with an entrance slit (S_{ent}), which is placed at the focus of a back collimating mirror (M_{coll}). Light collimated from this mirror is diffracted by the grating (G), and the now spatially separated wavelength components are then re-focused by a second mirror (M_{foc}) onto an exit slit (S_{exit}), which spatially filters out everything but a small wavelength band, which is detected. Monochromators typically use reflective elements rather than refractive ones, since they tend to be less dispersive. A scanning monochromator produces wavelength-resolved data by recording a detected signal, rotating the grating to vary the wavelength band passing through the exit slit, and repeating; commercially available optical spectrum analyzers common in the optical telecommunications industry are typically scanning monochromators.

The monochromator resolution is set by its linear dispersion and the width of the entrance and exit slits. Dispersion describes how well the monochromator spatially separates two different input wavelengths. It is usually specified in units of nm/mm, and is a function of the monochromator geometry and grating. For example, a 500 mm Czerny-Turner monochromator with a diffraction grating having a groove density of 1000 mm^{-1} may have a dispersion $\approx 1.5 \text{ nm/mm}$. If incoming light has been well-focused into the monochromator (input coupling is described in more detail below), so that the entrance slit width is equal to or smaller than the exit slit width and so that the beam completely fills the grating after being collimated by M_{coll} , the spectral resolution is approximately given by the product of the dispersion and the exit slit width. For example, for an exit slit width of $15 \text{ }\mu\text{m}$, the resolution is $(1.5 \text{ nm/mm}) \cdot (0.015 \text{ mm}) = 0.0225 \text{ nm}$. In this situation, the entrance slit does not affect the resolution, and the primary reason to reduce its size is to limit the amount of stray light that enters the spectrometer. In practice, it may not be possible to focus the incoming light as tightly as needed. In such situations, the entrance slit plays a role in determining the achievable resolution, as its size determines how well the grating is filled; if under-filled, spectral resolution may be lost. In general, a good procedure to follow is to measure the resolution by recording the spectrum from a narrow, monochromatic source. For example, a laser linewidth of 10 MHz ($\approx 5.6 \times 10^{-5} \text{ nm}$), achievable in an external cavity diode laser, will be below most monochromator resolution capabilities, so that the measured spectrum will essentially be an instrument response function.

A grating spectrometer is an instrument closely related to a monochromator. While a monochromator uses an exit slit and a single channel detector to detect one wavelength at a time, a spectrometer uses a multi-channel detector to acquire several wavelengths simultaneously, with each channel of the detector commonly called a pixel (since CCD detectors are often used). The

geometry of the Czerny-Turner can remain the same, with the exit slit opened all the way (or at least, to the lateral extent of the multi-channel detector). At a fixed grating position, the wavelength span that can be measured is equal to the product of the monochromator's dispersion, the pixel width, and the number of pixels. A 1024 element array with 25 μm pixel width will have a span of $(1.5 \text{ nm/mm}) \cdot (0.025 \text{ mm}) \cdot (1024) = 38.4 \text{ nm}$ if attached to the hypothetical spectrometer described above, and the best possible spectral resolution, approximately given by product of the pixel width and the monochromator's dispersion, is $\approx (1.5 \text{ nm/mm}) \cdot (0.025 \text{ mm}) \approx 0.0375 \text{ nm}$. As was the case with the single channel detector, measurement of the instrument response through a narrow linewidth source is a preferred way to determine the actual resolution of the system.

We next describe the entrance optics needed to take the collected emission (which we assume has been collimated) and feed it into the monochromator. Ideally, the entrance optics will ensure that the grating is perfectly filled (illuminated). If underfilled, loss of spectral resolution may result, while overfilling reduces the detected signal and can lead to unwanted scatter within the system. When ample signal is available, it is common to let the entrance slit S_{ent} do all of the work, in providing an aperture through which a diffracted beam is sent onto M_{coll} and through the rest of the system. As discussed above, the entrance slit width will then influence the achievable spectral resolution, and light will be lost as a result of the slit's aperturing effect. In this mode, there is a tradeoff between spectral resolution and throughput, and it is therefore not necessarily suited for high resolution measurements of small optical signals (e.g. single quantum dot spectroscopy). A focusing optic (L_{spec} in Figure 5) can be used to circumvent this tradeoff.

Monochromators are typically characterized by an f -number, which is a measure of the

collection angle of an optic (the higher the f -number, the lower the collection angle). To completely fill the grating, the ratio of the input optic's focal length to its input beam diameter should match this f -number. To be more concrete, let us consider two examples. The first assumes that a long working distance apochromatic objective has been used to produce a collimated collection beam with an 8 mm diameter, which is to be resolved in a f -6.5 monochromator. Matching the spectrometer f -number requires a 52 mm focal length optic. If a shorter focal length optic is used, the collimated beam should still be focused at the entrance slit, but will expand more quickly than is optimal, and will overfill the first mirror (M_{coll}), resulting in a net loss of detected signal. If a longer focal length optic is used, the beam will underfill mirror M_{coll} , and the optimal spectral resolution will not be achieved. As a second example, we consider light that has been collected into a single mode optical fiber. We expect to first collimate the light coming out of the fiber ($L_{\text{SMF,out}}$ in Figure 5) before focusing it into the entrance slit. The monochromator f -number of 6.5 corresponds to $NA \approx 0.077$, while the NA of the fiber is typically ≈ 0.14 , so as an initial guess, we expect to require a focal length ratio of about 1.8:1 (the NA ratio) for the two lenses. A more precise calculation is as follows: an $f_{\text{SMF,out}} = 11$ mm optic will produce a 2.6 mm collimated beam if placed at the output of a 7 μm mode field diameter fiber operating at 1.3 μm , so that a $f_{\text{spec}} = 17$ mm optic is needed to focus the collimated beam into the monochromator. This focal length ratio ($17/11 \approx 1.55:1$) varies from the initial guess because we have used the more precise Gaussian beam optics equation (Eq. 3) to calculate the collimated beam diameter, rather than the simple ray optics.

16.2.4.2 Detectors for measuring an emission spectrum

Factors to consider in choosing a detector include detection wavelength, sensitivity, single channel vs. multi-channel capability, and bandwidth. In the visible and short-infrared

wavelength region (350 nm to 1000 nm), silicon-based detectors are dominant, while in the near-infrared (e.g., 900 nm to 1700 nm), InGaAs and Ge detectors are commonly used. Single channel detectors can include p-i-n photodiodes, avalanche photodiodes, photomultiplier tubes, and single photon detectors. For photodiodes (often packaged with a transimpedance amplifier to produce an overall photoreceiver unit), the sensitivity will be limited by noise that is often specified as a noise-equivalent power (NEP), which includes contributions from noise sources other than photon shot noise, and is typically written in units of $\text{W/Hz}^{1/2}$, so that detection of an incident power equal to the NEP with a 1 s integration time will yield $\text{SNR}=1$. The minimum detectable signal is obtained for low bandwidths, limiting the ability to achieve ultra-sensitive detection with fast time resolution. Higher sensitivity can often be achieved in cooled detectors, where the cooling source is usually a thermoelectric Peltier element or a liquid nitrogen dewar. Such devices also tend to have much lower bandwidths than their uncooled counterparts. Detector noise usually scales with area, so it can be worthwhile to look for units that have as small an active area as possible without sacrificing detected signal. For example, if the exit slit width is going to be primarily kept at around 15 μm (to achieve good spectral resolution), a small area detector (e.g., diameter $\approx 50 \mu\text{m}$) with an appropriate focusing lens will ensure complete detection of the wavelength-resolved signal – there is no benefit to having a larger detector area. Lock-in detection is a technique that can often be used to improve the SNR in single channel detection. By using an optical chopper, for example, to modulate the detected signal, one can shift the detection away from DC to higher frequencies, away from many common noise sources.

Si CCDs and InGaAs photodiode arrays are common multi-channel detectors for spectroscopy, and as is the case for single channel units, cooling through a thermoelectric element or liquid nitrogen source is often used to reduce noise. A multi-channel detector can

provide significant benefit in comparison to a single channel detector in at least two ways. The most obvious is the multiplexed detection, i.e., the ability to simultaneously acquire information from multiple wavelength bins. In comparison to the step-and-acquire procedure when scanning the monochromator with a single channel detector, this multiplexed detection provides a time speed-up that is proportional to the array size along the wavelength-dispersed direction, which can often be in the range of 256 to 1024 elements. Considering that a 10 s integration may be needed to provide an adequate SNR level, the difference between producing one spectrum every 10 seconds and one every three hours is considerable. Next, although multi-channel detectors have a new noise source (readout noise) in comparison to their single channel counterparts, in some situations, the SNR is not limited by readout noise, but is dark count noise limited. One way to reduce dark count noise is to keep the detector size as small as possible without limiting the number of collected photons. The typical pixel size in a CCD is on the order of 25 μm x 25 μm , which is smaller than what is usually available in a single channel detector, but still large enough to capture the majority of the emission in the corresponding wavelength band, provided that the monochromator and its input optics are properly chosen. Furthermore, two-dimensional arrays such as Si CCDs usually have binning functions, so that multiple pixels in the vertical or horizontal directions can be grouped together. This can then allow the user to select a detector size appropriate to what is produced at the monochromator output.

The SNR available to a multichannel detector is limited by three primary noise sources: (1) photon shot noise, (2) dark count noise, and (3) readout noise. These values can typically be found within the manufacturer's specification sheet. If we call the detected photon flux (in units of counts/sec) P_{det} , the dark count rate (also in units of counts/sec) D , and the readout noise R_{rms} (usually provided as a root mean square value in units of counts), the SNR is given by:

$$SNR = \frac{P_{\text{det}} t_{\text{int}}}{\sqrt{P_{\text{det}} t_{\text{int}} + D t_{\text{int}} + R_{\text{rms}}^2}} \quad (9)$$

where t_{int} is the integration time. The above formula, which implicitly assumes that we have included the detector response (quantum efficiency and gain) into P_{det} and D , shows how a measurement can be noise-limited in different regimes. For a short enough integration time, we expect readout noise to be the dominant contribution, while at a longer integration time, some combination of dark count noise or photon shot noise will dominate. Clearly, the preference is to be photon shot noise limited, where $SNR \approx \sqrt{P_{\text{det}} t_{\text{int}}}$ and continues to improve with either increasing P_{det} or t_{int} . While shot noise limited detection is often achievable at visible wavelengths with Si-based detectors, in the near-infrared, it can be harder to achieve in low light level experiments (e.g., single emitter PL measurements), due to lower gain and orders of magnitude higher dark count rates in InGaAs detectors. Particular attention must therefore be paid to efficient photon collection in the construction of near-infrared micro-PL setups. Finally, it should be noted that the pixels in a multichannel detector are typically specified to have a certain full well capacity, which is the maximum number of counts supported by the detector at a given gain setting. The full well capacity limits both the dynamic range of a measurement and the maximum integration time over which an experiment can be conducted. Even though eq. (9) indicates that the SNR improves indefinitely with increasing t_{int} , in practice t_{int} will be limited, and the values of P_{det} and D will determine the maximum achievable SNR . Finally, it should be noted that detectors may have additional noise sources not included in eq. 9; for example, charge multiplying CCDs have an “excess noise factor” that must be taken into account (Robbins 2003).

16.2.4.3 Detectors for studying time-dependent phenomena

Until now, we have been concerned with detectors for acquiring a PL spectrum. In such measurements, low noise and single vs. multi-channel capability are the main concerns, and the

detector bandwidth need only be fast enough to respond to the acquisition time, mechanical chopper speed, etc. Of course, the energy level structure mapped out by a PL spectrum only tells part of the story – information about the PL dynamics can also be quite important, and is discussed in detail in Chapter 12. The process by which one measures spectrally-resolved dynamics is conceptually straightforward. A pulsed laser excites the material under study, and the scanning monochromator is used to select a wavelength band from the resulting emission, which is then studied with a sufficiently high bandwidth detector to obtain the desired temporal resolution. The process is then repeated for a new wavelength band, and after several iterations, a two-dimensional map of PL intensity against wavelength and time is produced.

In considering the detectors to use for such a measurement, we recall that photoreceivers based on p-i-n and avalanche photodiodes are usually specified with a bandwidth and NEP, which correspondingly set the best possible temporal resolution and sensitivity at that temporal resolution. For the low light levels associated with many micro-PL experiments, these detectors are simply not sensitive enough; a gain of 10^7 may be possible, but at a bandwidth of less than 100 Hz. A photomultiplier tube (PMT) is an instrument that can typically provide very high gain (in the 10^7 range) while simultaneously maintaining a temporal resolution in the ns or even sub-ns range, making it a more suitable choice in many situations. Single photon counters are an important alternative to PMTs for measuring ns-scale dynamics at low light levels. As the name implies, these detectors are sensitive enough to register single photon events, which is done by biasing an avalanche photodiode above its breakdown voltage (Geiger mode operation), and sub-100 ps resolution can be achieved in some commercially available detectors. The output of the single photon counter is usually an electronic pulse for each detection event.

Such time-domain measurements are discussed in detail in Chapter 12, so we provide just

a few comments here. The first is that if the pulsed laser source has a repetition rate R and pulse width p , and one wants to study the dynamics of a system with a characteristic decay time τ , One must have $p \ll \tau \ll 1/R$, so that each laser pulse initiates a new lifetime trace. The traces are then averaged to generate the final measurement result, with averaging and data acquisition done in different ways depending on the detection equipment used. With standard photodiodes, for example, an oscilloscope or fast data acquisition card that is appropriately synchronized (triggered) to the excitation pulses can be used. This synchronization is produced by an electronic trigger signal that is usually provided as an output from the pulsed laser source. With a single photon detector, a different set of electronics is required, the sum total of which is usually referred to as a time-correlated single photon counting (TCSPC) setup (Becker 2005) (Chapter 12). Recently, many commercial vendors have begun to offer TCSPC systems that integrate the needed electronics into a single unit. Included in such units are discriminators that measure the arrival times of the electronic pulses generated by the excitation source and detected photon, a time-to-amplitude converter (TAC) to measure the time difference between them, and an analog-to-digital converter (ADC) to digitize the signal from the TAC and produce a histogram showing the number of detected events as a function of time difference. To reduce noise, it is sometimes appropriate to use the electronic trigger signal from the laser not only on the electronic data acquisition end, but on the detection end itself, to trigger a detection window (essentially, a gate that turns the detector on for time intervals on the order of τ , and at a rate R). Gated detection is commonly used with near-infrared InGaAs single photon counters (Ribordy 1998), where the avalanche photodiode is periodically biased so that it operates in Geiger (single photon detection) mode for specified short intervals at a specified repetition rate.

A different approach to lifetime measurements involves a streak camera, again discussed

in Chapter 12. The streak camera performs a time-of-flight measurement in which differences in time are mapped to differences in spatial position. This is done in two steps. First, upon illumination, a photocathode generates a number of electrons proportional to the intensity of the incident light. These electrons are fed into a region where a high speed sweep (synchronized by the excitation laser's trigger signal) is applied between two electrodes. This causes the electrons, which have different arrival times depending on when they were incident on the photocathode, to be mapped to different positions on a phosphor screen. Spectrally resolved measurements can be performed simultaneously by coupling a wavelength-dispersed signal into the streak camera. This will produce a two-dimensional image on the phosphor screen, where time is mapped along one axis and wavelength is mapped along the other. The temporal resolution of streak cameras can be in the sub-ps range, exceeding what can be done in most TCSPC measurements, and the sensitivity can be good enough to perform measurements on single emitters (Santori 2002).

Photon correlation measurements are another common time-domain characterization technique used in micro-PL setups. These measurements provide information on the statistics of the fluorescence, which can be used to characterize whether the source is incoherent (e.g., a blackbody radiator), a coherent Poissonian source such as a laser, or a truly non-classical light source as one might expect for a single emitter (Mandel 2005). The latter point is of particular relevance to micro-PL setups used for single emitter spectroscopy. Depending on the density, there can be many emitters within a diffraction limited spot, and although there can be spectral indications as to whether more than one emitter is producing fluorescence, these indicators usually rely upon arguments related to their inhomogeneous and homogeneous linewidths, which can vary from sample to sample. On the other hand, a measurement of photon antibunching (Mandel 2005, Michler 2003) in the second order correlation function (an intensity correlation

measurement) is an unambiguous demonstration of single emitter fluorescence. This normalized intensity correlation function $g^{(2)}(\Delta t)$ relates detection events separated by an interval Δt , and is given by:

$$g^{(2)}(\Delta t) = \frac{\langle I(t)I(t+\Delta t) \rangle}{\langle I(t) \rangle \langle I(t+\Delta t) \rangle} \quad (10)$$

The brackets denote ensemble averages, which, in a quantum mechanical picture, are expectation values (the expression also invokes normal ordering and time ordering, see Ref. [Mandel 1995]). Antibunching occurs when $g^{(2)}(\Delta t=0) < g^{(2)}(\Delta t > 0)$, while $g^{(2)}(\Delta t=0) \geq 1$ is expected for a classical source. Physically, this signifies the fact that in a single optical transition, when an electron is promoted from the ground state to the excited state, only one photon can be produced at a time – there should be no chance of detecting a second photon coincident with the detection of a first one. Antibunching measurements have been demonstrated in a number of systems, including single atoms (Kimble 1977), molecules (Basche 1992), colloidal quantum dots (Michler 2000), impurity color centers (Kurtsiefer 2000), and semiconductor quantum dots (Michler 2003).

The typical setup for a $g^{(2)}$ measurement is called a Hanbury-Brown Twiss (HBT) interferometer (depicted in the detection block of Figure 2), and involves the use of a 50/50 beamsplitter to separate the emitted light into two paths, each of which is fed into a single photon detector. The outputs of the two single photon detectors are fed into a TCSPC setup as described earlier, where now the start and stop signals into the TAC are generated by the two detectors, and a histogram of number of coincidence counts as a function of time delay is built up. Unlike the lifetime measurement, we note that a $g^{(2)}(\Delta t)$ measurement can be performed under either continuous wave or pulsed excitation, and conceptually, one might expect to obtain much of the same information from either approach. In practice, signal-to-noise considerations may favor the pulsed approach (particularly if gated detection is applied), though the difference in carrier

dynamics between the two excitation methods may produce distinct phenomena.

While $g^{(2)}(\Delta t)$ is an auto-correlation measurement on the emission within a single wavelength band, there can also be benefits to studying the cross-correlation between different wavelength bands. In semiconductor quantum dots, a spectrum such as that in Figure 12(a) shows the emission from many states, with no information as to the time-ordering of the emission. Cross-correlation measurements provide this information (Aspect 1980), and radiative cascades in quantum dots have been measured (Moreau 2001). The main difference in the setup required for the cross-correlation measurement is in the spectral filtering. In the auto-correlation measurement, a single spectral filter can be used before the 50/50 beamsplitter. In the cross-correlation case, spectral filters must be placed in each arm of the HBT interferometer.

16.2.5 Imaging

In this section, we consider white light imaging, used to resolve the surface of the sample upon which micro-PL measurements are being done (Figure 6). For micro-PL conducted in a commercial confocal fluorescence microscope, this type of imaging may be naturally included. In a home-built system, there are many factors involved, starting with an evaluation of the importance of imaging to the experiments at hand. In some situations, such as when performing micro-PL measurements on unprocessed materials, it may be enough to ensure that the pump spot is focused on the sample surface, and a fixed field of view with modest resolution will be adequate for this task because the spatial resolution of the measurement will be determined by the pump spot size and how finely the pump beam (or sample) is rastered from point-to-point. On the other hand, when performing micro-PL on processed devices, it can be necessary to have micrometer-scale spatial resolution in the imaging in order to properly align the pump beam with respect to a fabricated feature. The spatial resolution Δl is basically set by the wavelength and

the numerical aperture of the optic, as described in equation (8) ($\Delta l \approx 0.61\lambda/NA$).

In most cases, the imaging path will at least partially coincide with either or both of the pump and collection paths, and because maximizing the collected signal is typically the most important criterion, the choice of optics to image the sample will necessarily be constrained. Nevertheless, imaging needs can influence the decision. For example, in the apparatus in Figure 2, a single optic (*OBJ*) is used for focusing and collection in the excitation, collection and imaging paths. If only the first two were required, an achromatic doublet or an asphere may be adequate. However, the need for relatively high resolution white light imaging suggests using a high *NA* apochromatic optic, and along with the working distance considerations previously discussed, pushes the balance towards a long working distance microscope objective.

Assuming the primary focusing and collection optic is chosen in this way, there is still considerable flexibility in determining the rest of the imaging system. A number of options are available for the illuminating white light source, including bright white LEDs, fiber optic illuminators that use quartz halogen or metal halide bulbs, and ring lights that provide diffuse lighting. The orientation of the illuminator strongly depends on the properties of the sample and the environment in which it is probed. For opaque materials, reflection of the white light (episcopic mode) is usually done, while in transparent substrates, backside illumination through the sample (diascopic mode) is used. In episcopic mode, there is the possibility of keeping the illuminator off-axis, though the microscope objective and sample environment (e.g., within a vacuum chamber or cryostat) can limit how efficiently this approach can work. Normal incidence illumination, where the white light is sent through the microscope objective using a beamsplitter or mirror, is an option in such cases (Figure 6). Depending on the characteristics of the white light source and the distance between its output and the microscope objective, focusing

the illumination through a condenser lens (L_{wl} in Figure 6(a)) may be useful. The illumination source can affect the material under investigation (e.g., through absorption and subsequent carrier generation), so it is usually prudent to block it during a measurement.

Light reflected off the sample goes back through the objective before proceeding through imaging optics and into a camera, usually a Si charge-coupled device (CCD). A number of options exist, ranging from inexpensive (<\$50) cameras more commonly used for surveillance purposes, to several thousand dollar (or more) imaging cameras with good enough sensitivity to detect single molecule fluorescence. The chip size (number of pixels), sensitivity, frame rate, and display method are some of the important factors to consider. Along with the objective and imaging optics, the chip size determines the field of view imaged, and in some cases, the pixel size influences the achievable spatial resolution. The rate at which the camera acquires information (its frame rate) can be important in certain situations, though in general micro-PL setups do not require video rate streaming. Typically, the output of the camera (usually a video signal with a standard format like 75 Ω BNC, composite video, or S-video) is sent to a monitor for display, although such an approach does not allow for image acquisition. This can be done through various computer graphics cards or frame grabbers. In recent years, CCD cameras using the universal serial bus (USB) or Firewire computer interface have become available, allowing for the image to be displayed on a standard computer. This can be advantageous in systems for which a computer is already being used, as image acquisition is then readily available. In other setups, particularly when the imaging is not critical, acquisition is not needed and an inexpensive analog monitor (<\$100 for a black and white monitor) provides an adequate solution.

In considering image formation on the camera, we focus on the situation in which an infinity-corrected microscope objective has been used. The parallel rays produced by the

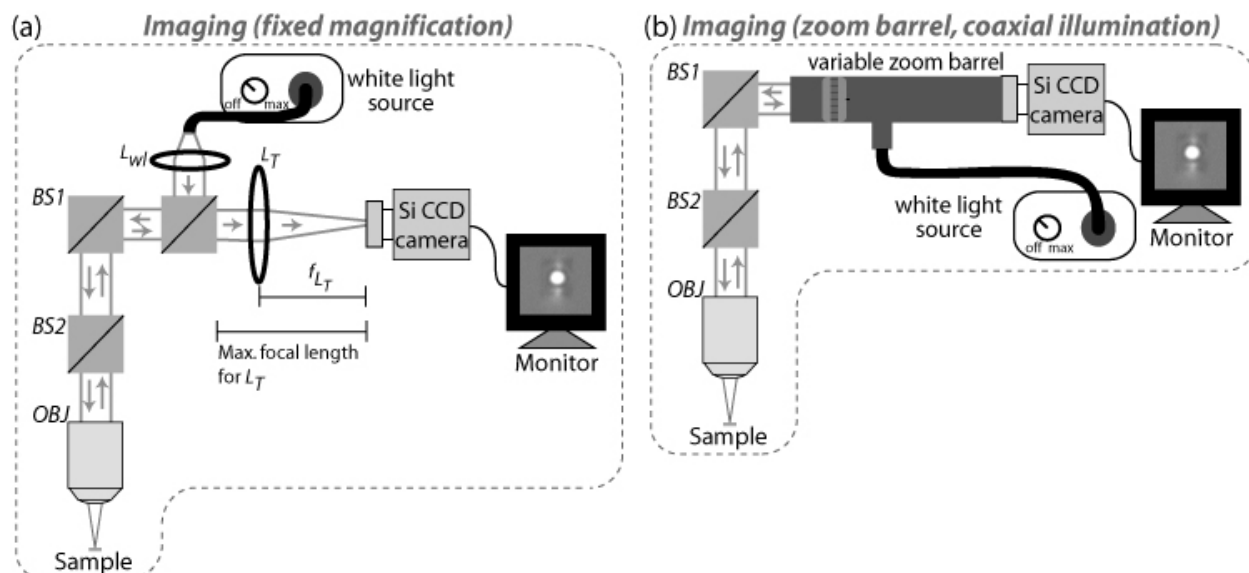


Figure 6: White light imaging block of a micro-PL setup; (a) fixed magnification determined by lens L_T ; (b) variable magnification using an adjustable zoom barrel with coaxial illumination.

objective are focused by a lens L_T onto the CCD, as shown in Figure 6(a). The field of view (FOV) imaged is given by the ratio of the CCD chip size to the magnification of the composite optical system consisting of the objective and imaging lens. If the objective has a focal length f_{OBJ} and the imaging lens has a focal length f_T , the magnification is given by the ratio $M = f_T/f_{OBJ}$, with the upper bound on M set by the amount of space available (if $f_{OBJ} = 10$ mm and $M=20$ is needed, $f_T = 200$ mm) and the intensity of white light available. A 1/2" CCD chip has dimensions of 6.4 mm x 4.8 mm (the 1/2" designation does not refer to the chip size, but is rather a historical artifact), so that a system with 20X magnification will have FOV=320 μ m x 240 μ m. Pixel size varies, but a typical 1/2" CCD has 640 x 480 pixels, so that the each pixel is responsible for an area of 0.5 μ m x 0.5 μ m, which is close to the minimum resolvable length scale set by the microscope objective (Δl). For the sharpest imaging, we want to be in the limit where each pixel samples an area much smaller than Δl . To do this, we need a higher level of magnification, while on the other hand, a larger field of view would require lower magnification. An alternate way of thinking of this is in terms of matching the actual CCD pixel size to Δl . In

this case, the pixel size is $20\ \mu\text{m} \times 20\ \mu\text{m}$, and if the microscope objective $NA=0.4$, $\Delta l=0.69\ \mu\text{m}$ for $\lambda=550\ \text{nm}$. This means we need a magnification of around 30X to have one pixel per Δl . In practice, a higher level of magnification (say 100X) is needed for adequate sampling.

Obviously, the magnification can be adjusted through replacement of the microscope objective and the eyepiece or lens tube, and for fixed FOV imaging this is the most straightforward approach. Since replacement of the objective changes the pump and collection areas, it is probably more desirable to change the eyepiece or lens tube. In some cases, however, it is necessary to switch between different FOVs. An example might be micro-PL measurements on microcavity arrays, where a large FOV is desired when imaging the array of devices, and ascertaining the position of a single device within the large array, but a small FOV is needed when interrogating a specific device. In such circumstances, a zoom system, commonly used in machine vision applications, might be used (Figure 6(b)). The zoom barrel is an adjustable focal length system that provides for a range of possible magnifications, and can usually be outfitted with additional tube adapters to increase the level of magnification possible. As an example, the zoom system we use in our setup has a magnification range between $\approx 10\text{X}$ and 130X when combined with the 20X microscope objective. The resulting FOV range is $640\ \mu\text{m} \times 480\ \mu\text{m}$ to $49\ \mu\text{m} \times 37\ \mu\text{m}$ for a $1/2''$ CCD camera, and as discussed above, 130X magnification provides adequate sampling for achieving the highest possible spatial resolution with the chosen objective.

16.2.6 Sample/objective positioning

Up to this point, we have discussed topics that fundamentally limit the achievable spatial resolution, such as the pump spot and area from which light is collected, but we have not described how to use this spatial resolution to construct a spatial PL map, or somewhat less ambitiously, how to effectively move from location to location so that the PL can be

characterized in different regions. Conceptually, one can envision either rastering the pump and collection paths or moving the sample, and each method has its strengths and disadvantages.

From an optics perspective, moving the sample is easier in that it in principle requires no adjustment to the pump or collection optics, provided that sample translation is purely within the plane orthogonal to the optical path, so that it stays in focus at all times. Motorized stages can provide nm-scale translation distances, so that the minimum step can be much less than the pump/collection area limited spatial resolution, and the same stages can offer several mm of translation, so that large sections of the sample can be covered. These attributes have led us to adopt sample translation as the primary method for producing spatially resolved PL maps in our micro-PL setup. There are some important disadvantages to keep in mind. Though translation stages are relatively stable, they will almost always be less stable than a completely monolithic sample mount. They are also much more costly, particularly if both high resolution and relatively long translation ranges are needed. Cost and stability become even larger concerns if the sample is to be interrogated in a non-ambient environment such as in a cryostat. In this case, cryogenically-compatible motorized stages can be used to translate the sample within the cryostat, or alternately, large platform (and load capacity) stages can move the entire cryostat.

Rastering the pump and collection optics consists of moving the primary focusing/collection optic, and then adjusting the corresponding mirrors to re-direct the pump and collection beams through it. To some extent, one might imagine being able to automate such a process through motorized optics mounts, and over relatively small translation ranges (e.g, several micrometers) the amount of adjustment needed is relatively small. Moving over more significant distances does require significant re-alignment, and can be a tedious process. As mentioned above, in our setup, we primarily use sample translation, but have also allowed for

some amount of pump/collection beam movement, through a stable and relatively high resolution manual translation stage to position the long working distance objective. It is important to have some ability to adjust the pump and collection beam paths, if only to ensure that the focus is properly set on the sample surface, and small adjustments of the pump beam position can be made through the initial turning mirrors, without having to re-align the collection optics.

16.2.7 Alignment and Calibration

Sections 16.5.1 and 16.5.2 provide tips for aligning optical systems, using the example of coupling into a single mode optical fiber. The alignment of the micro-PL setup roughly follows the same approach, but in multiple stages. A general procedure is as follows: (1) Approximately place the optical components of the micro-PL setup. Check their heights so that they lie along a common optical axis, and position lenses and objectives at the appropriate focal length/working distances. (2) Place the sample at the appropriate working distance with respect to the objective, and approximately align the imaging sub-section so that the white light source is focused onto the sample surface and the reflection can be observed in the CCD camera. It is often useful to image the edge of the sample to get the system into focus. (3) Collimate the excitation source, direct it into the objective, and observe the pump spot with the imaging sub-section. Small adjustments to the imaging components (e.g, camera/lens position) and the separation between objective and sample surface may be needed. The net result should be that the imaging system simultaneously displays both a tightly focused pump spot and an in-focus image of the sample surface. (4) Try to detect the reflected pump beam in the spectrometer (or whatever detector is being used). This will likely require temporary removal of the pump beam removal filter, in which case attention should be paid to how much power is put into the spectrometer, so as to not damage the detector. Using the methods of Section 16.5.1, maximize the detected signal. If

needed, keep the slit widths open as wide as possible to increase throughput (in the beginning, spectral resolution is not needed). (5) Once the pump beam detection has been maximized, re-insert the pump beam removal filter and try to measure the PL signal. Once any signal has been detected, the input optics to the spectrometer can be adjusted to maximize this signal.

When performing experiments with the micro-PL setup, it is important to have some sense for the source and magnitude of the uncertainties in the measured quantities. Clearly, there are noise sources associated with detection (and discussed in Section 16.2.4.2) that are important, but they are not our focus here. Instead, we focus on aspects related to system alignment, which can be significantly reduced through careful calibration. The basic result of a PL measurement is the emission level as a function of wavelength at a given pump power. We therefore focus on how one calibrates emission wavelength, emission level, and pump power.

Wavelength calibration is done through alignment of the grating spectrometer, which is usually a standard procedure performed when first setting up the machine. It typically involves use of a lamp source, such as Ar or Ne, which produces a series of spectral lines at well-known wavelengths that the spectrometer-determined wavelengths are calibrated against – some systems allow for such calibration to be implemented into the operating software. Next, the emission level read by the spectrometer can be calibrated with a laser source and calibrated power meter. The output of the laser source is first measured with the power meter, and then directed into the spectrometer using the input coupling optics as described in Section 16.2.4.1. The integrated photon count rate in the resulting emission spectrum is compared to the value produced by the power meter, providing an estimate of the spectrometer throughput that can be checked against the product of the vendor-specified grating efficiency, mirror reflectivities, and detector quantum efficiency. This throughput should be periodically checked to ensure that the system remains

calibrated. As discussed in Section 16.2.4.1, the use of a narrow linewidth source is also important in establishing the system's spectral resolution. Finally, as mentioned in Section 16.2.2, the pump power is typically detected at some reference position, so that the power at the sample surface is determined by placing the power meter at the sample position, reading the power level, and comparing it to the power level when the meter is placed at its reference position. Like the spectrometer calibration, this measurement must be done periodically.

16.3 Measurements using a micro-PL setup

Having described the construction of a micro-PL setup, we now present a sampling of the data that can be acquired from such a system. In Section 16.3.1, we discuss measurements on microcavity lasers, while in Section 16.3.2, we discuss quantum dot spectroscopy.

16.3.1 Microcavity lasers

Microfabricated structures often require spatially-resolved optical measurements, and microcavity lasers are one example of such a device. The results reviewed in this section were reported in (Srinivasan 2003), in which photonic crystal (PC) membrane microcavities were fabricated in a material containing InAsP/InGaAsP quantum wells on top of an InP sacrificial layer, designed for 1300 nm emission. The devices (Figure 7) have in-plane dimensions of $\approx 8 \mu\text{m} \times 11 \mu\text{m}$ and a thickness of 252 nm, and the spacing between devices is 20 μm .

The devices were tested in a micro-PL setup similar to that depicted in Figure 2, where a 20X magnification, long working distance microscope objective (OBJ) was used for pumping, collection, and imaging. The sample was kept in atmosphere and pumped with an 830 nm laser diode. To correct for the severe astigmatism of the diode's output, an anamorphic prism pair was used, though the result of the circularization (Figure 7(c)-(d)) was imperfect. Heating of the membrane due to absorption of the pump beam limited the maximum pump power that could be

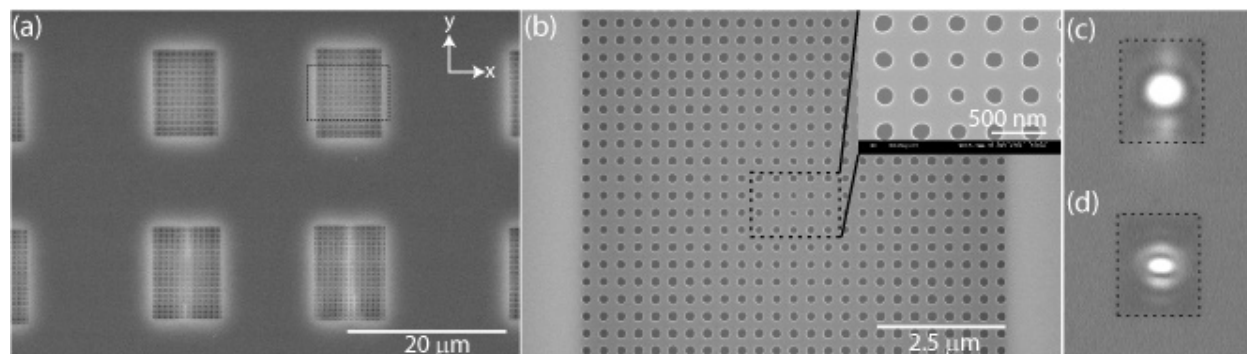


Figure 7: (a)-(b) SEM images of photonic crystal (PC) microcavity laser array. (c)-(d) CCD images of the excitation spot under (c) diffuse and (d) focused pumping conditions, obtained using the zoom barrel imaging subsection of the micro-PL setup described in this chapter. The cavity boundary is shown as a dotted line for reference. Parts (b)-(d) reprinted with permission from (Srinivasan 2003). Copyright 2003, American Institute of Physics

used, since the PC cavities are membrane structures with limited thermal contact to the rest of the chip, and would collapse upon absorption of too much average power. This necessitated pulsed excitation, which was accomplished by a pulsed voltage source that drove the laser diode with a pulse width of 10 ns and period of 300 ns. The collected light was separated from the residual pump beam by a free-space edge pass filter, focused into a multi-mode optical fiber (core diameter = 62.5 μm), and wavelength-resolved using an optical spectrum analyzer (OSA). The OSA was essentially an automated scanning monochromator incorporating a single channel InGaAs detector. The minimum collected power that can be measured with this instrument was

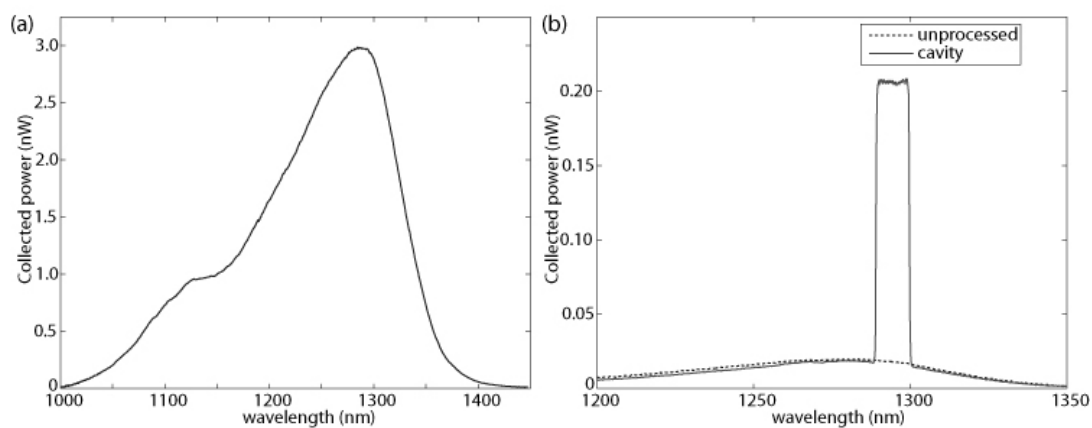


Figure 8: (a) PL spectrum from the quantum well material prior to fabrication; (b) PL spectrum from a PC cavity (solid) and an unprocessed region of the chip to the side of the cavity (dashed). Wavelength resolution = 10 nm.

around 1 pW, with a spectral resolution as high as ≈ 0.1 nm. Figure 8(a) shows a reference PL spectrum collected from an unprocessed portion of the material, under strong cw excitation (≈ 1 mW), with a wavelength resolution of 10 nm, and a focused pump spot area of $8 \mu\text{m}^2$ (Figure 7(d)). A broad wavelength resolution was chosen to maximize the collected signal and because no sharp features were expected. This reference spectrum reveals a few important pieces of information about the material: the peak emission wavelength (1287 nm), the width of the ground state emission peak (≈ 140 nm), and the presence of a second (excited) emission peak at 1125 nm. The peak emission wavelength informs the choice of fabricated PC lattice constant (a) and hole radius (r), as simulations of the employed graded lattice geometry specify that $a/\lambda \approx 0.25$ and r/a should vary between 0.23 and 0.31. Since the material emits across a range of wavelengths, cavities of different geometries (and hence different resonant frequencies) can be observed, and it is common practice to check theoretical expectations by confirming the predicted change in cavity emission wavelength as a function of a and r . The spectrum from one cavity (now under pulsed excitation at an average pump power of a few μW) is shown in Figure 8(b), along with PL from an unprocessed region of the chip to its side. The spectra line up closely, with the cavity spectrum showing a peak at $\lambda \approx 1294$ nm.

Having obtained a broad picture of this device's spectral behavior, we now focus on learning more about the cavity mode emission. By adjusting the wavelength resolution of the OSA (corresponding to a reduction in the monochromator slit width), we find that the observed peak contains a single mode that is quite narrow (inset of Figure 9(a)), and in fact is narrower than the best resolution of the OSA (0.10 nm), provided that heating effects in the membrane are mitigated through use of a more diffuse pump beam (Figure 7(c); area $\approx 21 \mu\text{m}^2$).

As discussed in (Srinivasan 2003), if the emission linewidth is measured at the pump

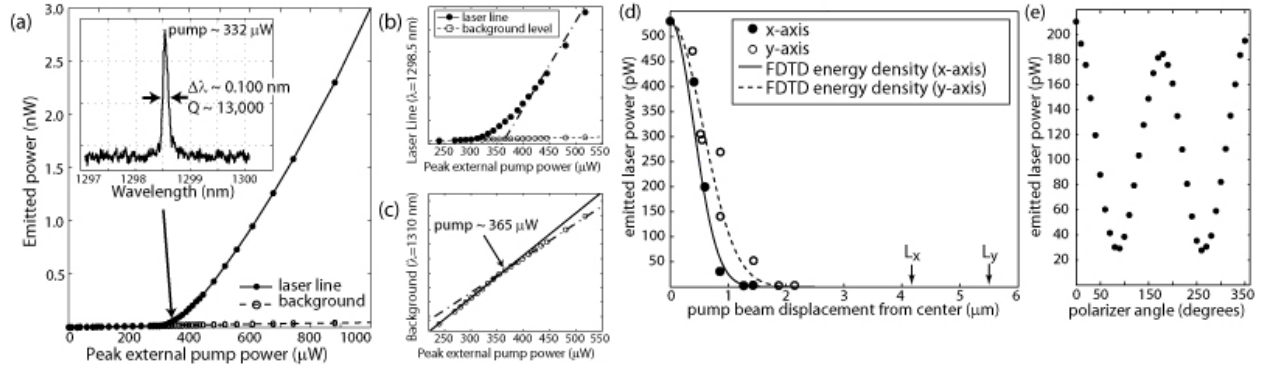


Figure 9: (a) L-L curve and sub-threshold spectrum (inset) of the PC microcavity pumped, and zoomed-in plots of (b) laser threshold and (c) background emission. (d) Laser power as a function of pump position along the x and y axes of the cavity. Finite difference time domain (FDTD)-generated Gaussian fits to the envelope of the electric field energy density of the cavity mode are shown for comparison. L_x and L_y correspond to the physical extent of the PC in the x and y direction, respectively. (e) Emitted laser power as a function of polarizer angle with respect to the x axis of the cavity. Figure reprinted with permission from (Srinivasan 2003). Copyright 2003, American Institute of Physics

power at which material transparency is reached, an estimate of the cavity quality factor (Q) is obtained (Q is a measure of the photon lifetime in the cavity). The light-in-light-out (L-L) curve (Figure 9(a)-(c)), given by measuring the emission in the cavity mode as a function of pump power, shows the characteristic turn-on of a laser (Yariv 2007), with the relatively smooth transition (rather than an abrupt kink) indicative of a microcavity, in which the number of modes involved is far less than in a macroscopic device. Extrapolating back from the data at high pump powers gives an estimate of the laser threshold, which in this case is 360 μW . Measurement of the background emission, produced by gain regions external to the cavity, as a function of pump power (Figure 9(c)) indicates (incomplete) gain clamping, with the kink at $\approx 365 \mu\text{W}$ coinciding with the extrapolated laser threshold value.

The sub-threshold spectrum and L-L curve are perhaps the two most common measurements used to characterize microcavity lasers in a micro-PL setup, but there are several other pieces of information that can be obtained. Figure 9(d) shows the emitted power as a function of pump beam position on the cavity, where the position was varied by moving the

sample. This measurement provides qualitative understanding of mode localization in such a device, and illustrates why spatial resolution smaller than the cavity size might be useful – we explicitly see the ability to spatially resolve emission with a resolution of $\approx 1 \mu\text{m}$, which is ten times smaller than the cavity size. Next, the polarization of the laser emission is determined by placing an adjustable polarizer in the collection path, for example, between BS2 and OBJ in Figure 4. Figure 9(e) shows the collected emission as a function of polarizer angle with respect to the cavity's x -axis, confirming that the emission is x -polarized, as expected from calculations.

Another important piece of information, not presented here, is the cavity linewidth as a function of pump power, which can provide information about gain and loss in the laser, but would require a higher spectral resolution device such as a scanning Fabry-Perot cavity, since the OSA resolution is insufficient. Correlation measurements, as discussed in Section 16.2.4.3, provide important information about the onset of lasing in a microcavity (Strauf 2006). Microcavities are typically distinguished by a relatively small number of optical modes, so that the transition between spontaneous emission and lasing in an L - L curve, marked by a pronounced kink in a macroscopic device, is not necessarily readily apparent. Indeed, as the number of optical modes is reduced to unity, this kink is expected to soften, and under certain conditions, disappear. To distinguish between such a device and one operating in the spontaneous emission regime, a measurement of $g^{(2)}(\Delta t)$ can be performed, and will show a transition as the emission becomes coherent. Measurements of $g^{(2)}(0)$ as a function of pump power can then be used to establish the laser threshold and probe the behavior of few mode microcavities.

16.3.2 *Quantum dot spectroscopy*

In this section, we discuss micro-PL measurements of self-assembled InAs quantum dots (QDs) embedded in GaAs that emit at $1.2 \mu\text{m}$ to $1.3 \mu\text{m}$, down to the single QD level. The

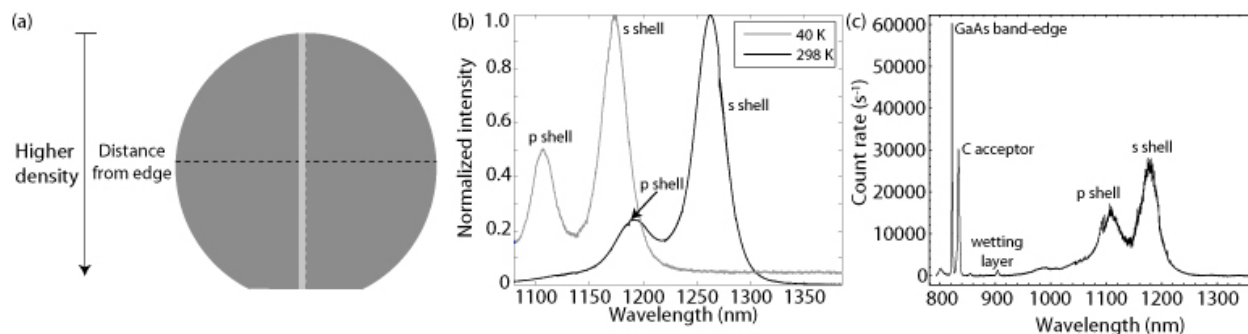


Figure 10: (a) Schematic of the quantum dot wafer with a density gradient along one axis; (b) 298 K and 40 K PL spectra from a high density region of the wafer, showing the ground state (s shell) and excited state (p shell) ensemble emission, and an ≈ 90 nm blue-shift between room and low temperature; (c) broad PL spectrum from a high density region of the wafer at 7K, showing the GaAs band edge, carbon acceptor peak, and wetting layer emission along with the QD ensemble s shell and p shell peaks.

apparatus used is similar to that of the previous section and is schematically depicted in Figure 2.

Our research investigates the interaction of QDs with tightly confined optical fields, and in such experiments, limiting the QD dephasing below some minimum value is required. This is done by cooling the sample to a temperature below 20 K using a liquid helium flow cryostat. The other important modification with respect to the measurements of Section 16.3.1 is the use of a grating spectrometer with a liquid-nitrogen-cooled InGaAs array detector, which as described in Section 16.2.4.2, substantially improves the SNR and measurement time with respect to a scanning monochromator and single channel detector. While the collected power levels in the previous section were in the pW to nW range, in these measurements collected signal levels are in the 0.1 fW to 10 fW range, necessitating the much more sensitive detector. Finally, we use two different laser sources in our measurements: an 830 nm cw (fiber-coupled) laser diode, and a 780 nm pulsed laser diode with a 50 ps to 100 ps pulse width and 50 MHz repetition rate.

We first consider measurements of QDs that emit at 1.2 μm . These structures, grown by molecular beam epitaxy, have a density gradient along one axis of the wafer (Figure 10(a)).

When interrogating a new wafer, our goals are to: (1) determine the peak emission wavelength of the ground state ensemble (knowing that the peak position may vary across the wafer), (2)

examine the PL as a function of position along the density gradient, ascertaining the portion of the wafer where single QD emission can be observed, and (3) perform additional measurements (pump-power dependent behavior, lifetime, $g^{(2)}(\Delta t)$) on single QDs.

Figure 10(b) shows PL spectra that have been taken from a high density region of the wafer, at temperatures of 298 K and 40 K. The pump beam diameter is around 5 μm , with an average incident pump power of 60 μW (wavelength=830 nm), and emission is collected from a 2 μm diameter portion of the excited region with a 1 s integration time. Both PL spectra show two dominant peaks, corresponding to the ground and excited states of the QD ensemble. In comparing room temperature and low temperature results, we note a couple of salient points. First, there is a wavelength blue-shift of about 88 nm, which follows the band-gap of the host semiconductor material (Vurgaftman 2001), and can be a qualitative check on the sample temperature (although the cryostat temperature sensor may read a certain value, poor thermal conductivity can sometimes prevent proper cooling of a sample). Next, we see that the linewidth of the peaks does not appreciably narrow at low temperature (the full-width at half maximum for the s-shell changes from 33 nm to 30 nm). This is because the peaks are inhomogeneously broadened due to the size distribution of QDs produced by the Stranski-Krastanov growth process (Michler 2003). In Figure 10(c), we show another PL spectrum from the sample, now at 7 K, over a much broader wavelength range. By pumping the sample at 780 nm and using an 800 nm edge pass filter to remove residual pump light, we are able to observe other important emission peaks (we also reduce the average pump power to 4 μW in preparation for single QD measurements). At 900 nm, we see emission from the QD wetting layer, a thin region of semiconductor material used to help seed the QD growth. At 833 nm, we see emission from the

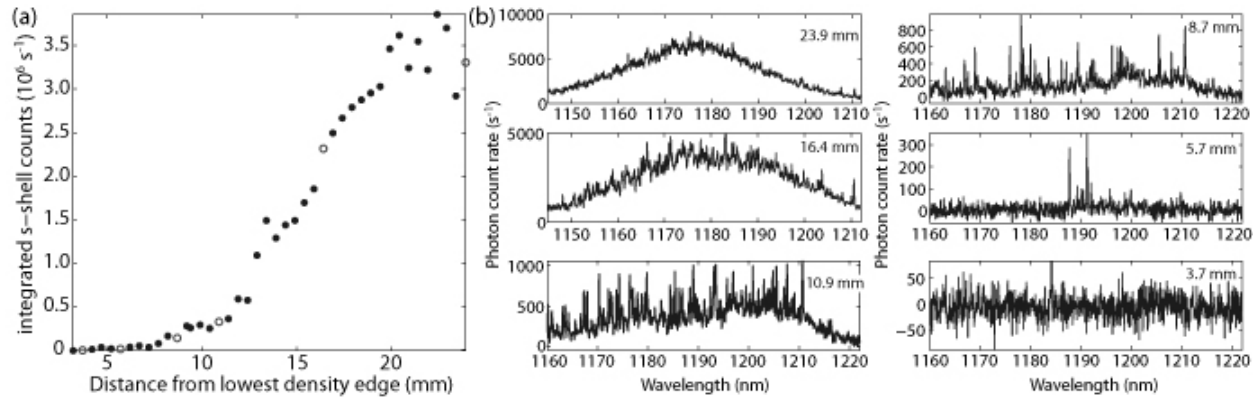


Figure 11: (a) Integrated s-shell emission as a function of position along the QD density gradient, taken at 7 K. Open circles denote positions for which full spectra are shown in (b). Single QD emission lines are observed at a distance of ≈ 4 mm to 7 mm from the low density wafer edge. Average incident pump power = 300 nW.

carbon acceptor impurity state, and at 823 nm, we see emission from the GaAs band-edge. The relative strength of these peaks provides information about the material under investigation. For example, the strength of the carbon acceptor peak can be indicative of the growth chamber conditions (how much carbon is in the chamber), while the GaAs band-edge emission can be less prominent in quantum well structures due to rapid relaxation of carriers into the wells.

Next, we look at the PL as a function of position along the direction of the density gradient and near the center of the wafer. Fixing the grating position so that it is centered about the s-shell, we pump relatively weakly (300 nW incident power), to reduce background emission created by QD/wetting layer carrier interactions, and acquire spectra with a 30-60 s integration time. A 0.5 mm step size is used to map PL across the wafer, but sub-micrometer resolution can be utilized if needed. The integrated s-shell emission as a function of position is shown in Figure 11(a), with spectra at selected positions shown in Figure 11(b). We observe two dominant trends. First, the integrated emission almost monotonically decreases as we approach the low density wafer edge, as one would expect, with essentially no emission once we are within 3 mm to 4 mm of the edge. Next, the character of the PL spectra begins to change. As we move to lower density regions, the broad emission curve is punctuated by a multitude of emission spikes,

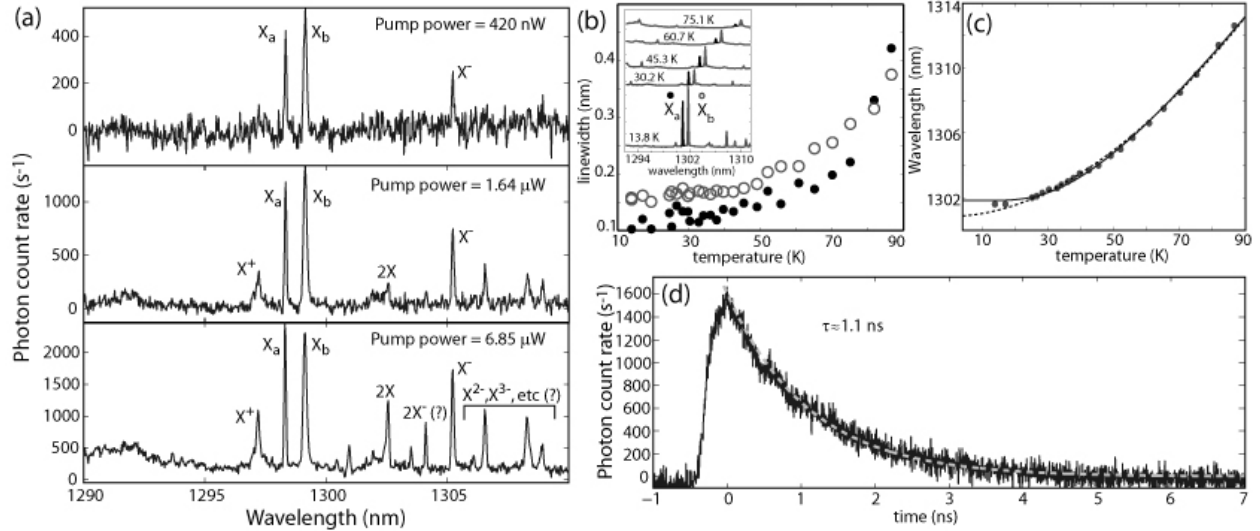


Figure 12: (a) PL spectra from a single QD for differing pump powers, with the QD states tentatively identified, taken at 7 K. (b) Linewidth of X_a and X_b as a function of temperature (spectra inset). (c) Position of X_b as a function of temperature (dots), with fits to the data using the Varshni (dashed) and Bose-Einstein (solid) functional forms. (d) PL decay and fit for emission from 1294-1306 nm, under weak excitation so that only X_a , X_b , and X^- are present. Part (b) reprinted with permission from (Srinivasan 2007). Copyright 2007, American Institute of Physics as the QD density becomes sufficiently low so that PL from small numbers of QDs can be resolved, rather than just the inhomogeneously broadened PL from the ensemble. At approximately 5.7 mm from the low density edge, we see essentially no broad ensemble PL, but instead only a few sharp peaks. These peaks correspond to states of a single QD, as has been described in a multitude of references (Michler 2003) (Chapter 2). Calculations that account for the shape and composition of the QD can help us distinguish between neutral, charged, and multiple exciton states. Pump power-dependent measurements can also provide useful information, in that the neutral exciton state is generally expected to exhibit emission at pump powers lower than that at which charged states will be present. In addition, the biexciton state is expected to have quadratic pump power dependence, in contrast to the linear dependence of the exciton (Chapter 2).

Such identification was presented in (Srinivasan 2007) for a different QD epitaxy (a

single quantum dot-in-a-well, or DWELL), though the focus there was on improved collection efficiency through use of a fiber taper waveguide probe. Figure 12(a) shows measurements of this DWELL material using the PL setup described above for 1.2 μm QDs. As was the case in (Srinivasan 2007), excitation at the lowest pump powers shows three emission lines, corresponding to the polarization split neutral exciton states (X_a/X_b) and negatively charged state (X^-) of the QD. As the pump power increases, additional states appear, including the positively charged state (X^+), and biexciton state ($2X$). At the highest pump levels, a multitude of states are expected, including multiply charged states (e.g., X^{2-}) and QD states that are hybridized with the wetting layer. Precise identification of these spectral lines through PL measurements (and supporting theoretical calculations) alone can be quite difficult. Placing the quantum dot in a field-effect structure to allow for capacitance spectroscopy (Drexler 1994) is a commonly-used method to provide a better understanding of the QD energy level structure.

Figure 12(b) shows data from (Srinivasan 2007), zooming in on the neutral exciton lines of such a QD and plotting their PL linewidths as a function of sample temperature, between 13.8 K and 90 K. The broadening of the linewidth corresponds to an increase in the QD dephasing, to be expected due to the increased interaction with phonons at higher temperatures; however, the limited spectral resolution of the system used precludes accurate measurements of linewidth below ≈ 25 K. Measurements with better spectral resolution (Bayer 2002) indicate that the broadening is essentially continuous as the temperature is increased above the lowest temperature achieved (2 K), and that the increase is roughly linear with a slope of ≈ 0.4 pm/K for temperatures below 60 K. Figure 12(c) shows the wavelength of the X_b line as a function of sample temperature (starting at 13.8 K), along with least squares fits to the data using the well-known Varshni and Bose-Einstein functional forms (Grilli 1992), which have seen widespread

use in investigations of the temperature dependence of direct bandgap semiconductors (Vurgaftman 2001). The data follows both curves reasonably well, again providing a qualitative check of the sample temperature (the linewidth of the QD lines is a second check). The plateau in the emission wavelength at lowest temperatures seems to fit the Bose-Einstein curve more closely, which has been suggested to be the case at temperatures below 80 K (Grilli 1992).

Finally, in Figure 12(d), we present a measurement of the PL decay from states of this single QD, using a setup similar to that discussed in Section 16.2.4.3. The sample is pumped with the aforementioned 780 nm pulsed laser, at an average power that excites only the X_a/X_b and X^- states, as in Figure 12(a). A 12 nm bandpass filter centered at 1300 nm removes emission outside of this wavelength band, and the signal collected by a single mode optical fiber is sent into an InGaAs single photon counter operated in gated detection mode with a 20 ns gate width and 10 μ s dead time, and whose output is sent to a TCSPC board. The trigger signal of the laser is fed to a digital delay generator, which serves as a master clock for the experiment, with one output triggering the gated detection mode of the single photon counter, and the other fed to the TCSPC board. The resulting lifetime trace (Figure 12(d)) is fit to a singly decaying exponential (in practice the logarithm of the curve is fit to a linear function), with a lifetime of $1.1 \text{ ns} \pm 0.1 \text{ ns}$. This decay constant is consistent with the 1 ns lifetime typically measured for InAs QDs (Michler 2003); more precise measurements could be made by using a narrower bandpass filter to study only one QD state at a time, and by improving the collected signal.

16.4 Related micro-optical techniques

In this section, we describe a few extensions to the micro-PL setup that can equip the user with the ability to probe additional aspects of the material system under investigation. The discussion below is by no means comprehensive, and because the optical techniques involved are

largely similar to those involved in micro-PL, less detail is provided.

16.4.1 Photoluminescence excitation (PLE) spectroscopy

The basic measurement performed in photoluminescence excitation (PLE) spectroscopy is that of the sample's emission spectrum as a function of excitation wavelength (Chapter 6). Until now, we have paid little attention to the excitation wavelength other than to say that it should be at a wavelength for which the sample has adequate absorption to generate the carriers needed to fill the relevant energy states that produce luminescence. There can be more to this story, however, as some materials may have spectrally narrow absorption bands, so that precise spectral alignment is needed, or absorption bands that lead to preferential emission on certain transitions. The InAs quantum dots described in the previous section provide one example where PLE measurements can be useful. The broad spectrum of Figure 10(c) indicates several luminescence centers other than the ground state of the QD ensemble, including the GaAs band-edge, the C acceptor peak, the quantum dot wetting layer, and the QD ensemble p-shell. The measurements we described so far were at pump wavelengths within the GaAs band-gap (780 nm excitation) or at the C acceptor peak (830 nm excitation), so that carriers were generated at much higher energies than the QD transition, and fluorescence at the QD ground state occurs only after carriers relax into the QD states. Pumping at a wavelength closer to resonance with the QD s-shell, for example, at the wetting layer (900 nm) or preferably, the QD p-shell (1100 nm), can produce different carrier dynamics that will physically influence the behavior of the system. For example, photon correlation measurements have been used to study sub-microsecond correlations in QD samples under above-band and near-resonant pumping (Santori 2004).

PLE measurements have recently been performed in (Badolato 2008), in a system

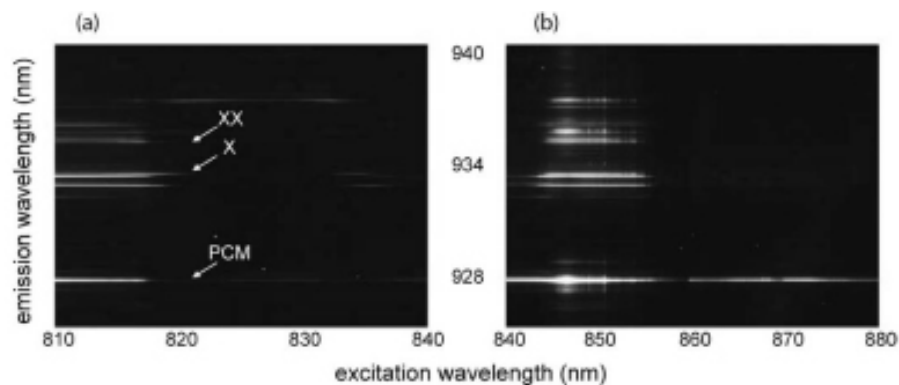


Figure 13: PLE spectra of a coupled cavity-QD system when tuning the excitation wavelength over the (a) 810 nm to 840 nm region (50 nW pump power), and (b) 840 nm to 880 nm region (500 nW pump power). Awaiting re-printing permission from Elsevier.

consisting of a single InAs QD in a photonic crystal microcavity for which there is only one cavity mode interacting with the QD. Data from this study, re-printed in Figure 13, shows how the PL intensity in the QD states and cavity mode varies with excitation wavelength and the corresponding photogenerated carrier density. For wavelengths below the GaAs band-edge (≈ 820 nm), PL is collected from the cavity mode¹ and the X and XX states. At excitation wavelengths between 820 nm and 840 nm, one can find regions in which the X/XX states are bright and the cavity is comparatively dark, and vice versa. The presence of carbon impurities at 833 nm (Figure 10(c)) suggests that excitation of these shallow acceptor states can generate electrons that readily fill the QD states, but do not contribute to emission into the cavity mode. Increasing the excitation wavelength to 846 nm produces bright emission from both the cavity and QD states, for reasons currently unknown, and a further increase beyond ≈ 860 nm (now in the region of the QD wetting layer) produces bright cavity mode emission but no emission from the QD.

From an equipment standpoint, the modifications to the setup in Section 16.2 (Figure 2) are straightforward, albeit potentially expensive. The main requirement is a tunable laser; a Ti:

¹ The source of the cavity mode emission when non-resonant with a QD state is an active area of research, and PLE measurements provide information about this, particularly when combined with photon correlation measurements.

sapphire or dye laser will generally provide the broadest wavelength coverage, a necessity if widely spectrally separated absorption centers are to be excited. The spectral resolution of the measurement will be limited by the excitation laser's linewidth. Changing the excitation wavelength may also require adjustment of the filter(s) used to separate the pump from the collected signal. For systems in which laser spontaneous emission is problematic, a tunable bandpass filter may be required at the output of the tunable laser.

16.4.2 Electroluminescence

Electroluminescence (EL) measurements are sometimes used to characterize systems in which electrical injection of carriers into the light-emitting transitions can be achieved. III-V semiconductors are perhaps the most notable example of this, and EL measurements are a necessity in the development of technologically important current injection devices, including microcavity lasers (Levi 1992) and single photon sources (Yuan 2002). Conceptually, EL measurements involve a replacement of the photoexcitation used in PL with current injection. The specifics of the injection scheme (e.g., wire bond vs. electrical probe) and the material design for efficient carrier generation are beyond the scope of this chapter, but in one common situation, an EL sample is made by placing the light emitting layer in the intrinsic region of a p-i-n diode. Once the applied bias is large enough, a current can pass between the doped layers in the intrinsic region (inset of Figure 14(a)). In this region, carriers can optically recombine, emitting photons that are detected in the same manner as in PL. To modify the setup described in Section 16.2 for EL measurements, in principle all that is needed is to ensure that the beam collection optics and the environment housing the sample are compatible with the current injection scheme. For example, electrical testing in a cryogenic probe station usually involves

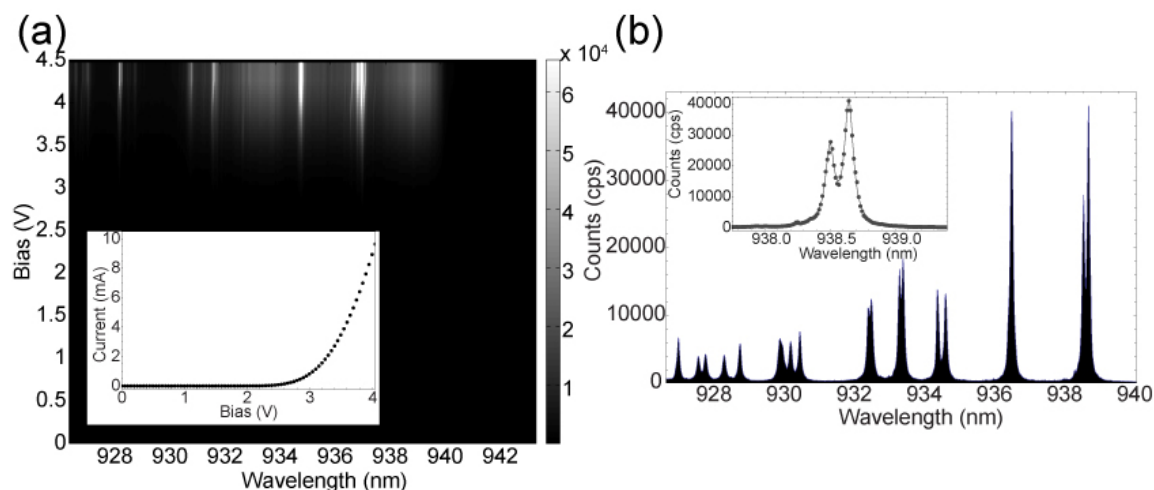


Figure 14: (a) Electroluminescence spectrum as a function of applied bias for an electrically gated micropillar cavity with embedded quantum dots. The dark, sharp lines are cavity modes and the weaker emission between modes is due to the QDs. The onset of luminescence coincides with the current turn-on in the IV curve (see inset). (b) Photoluminescence spectrum of the same device under no applied bias. Inset: A fit to the polarization-split fundamental cavity modes. Figure re-printed with permissions from Matthew T. Rakher, "Quantum optics with quantum dots in microcavities," PhD thesis, University of California, Santa Barbara.

long working distances, so that the apochromatic objectives discussed thus far remain a good choice, and in some cases, even longer working distance optics may be needed. On the other hand, a requirement of good collection efficiency and high numerical aperture optics with shorter working distances may necessitate the experimenter to explore wire-bonded geometries that maintain a smaller form factor.

To illustrate some of these concepts, we consider the EL spectrum from a QD embedded in a microcavity structure, as shown in Figure 14 (Rakher 2008). In this structure, a vertical cavity surface emitting laser (Coldren 1995, Yariv 2007) design was used to electrically contact a single micropillar cavity. In such a scheme, the top GaAs/Al_{0.9}Ga_{0.1}As stack was p-doped while the bottom stack was n-doped and the sample was grown on n-type GaAs. The p-type mirror was contacted using a Ti/Pt/Au metallization while the n-type mirror was contacted using a AuGe/Ni/Au metallization after etching. The sample was then wire bonded and placed in a cryostat at 4 K, a voltage-current source was used to apply an external bias, and the EL was

collected as a function of applied bias as shown in Figure 14(a). The turn-on of luminescence coincides with the turn on of current near 3 V (see inset). EL is detected both from the micropillar cavity modes (narrow, dark lines) and bare QD-related emission (underlying broad emission). This spectrum can be compared to the PL spectrum from the same device under no applied bias, as shown in Figure 14(b). The broad QD emission is significantly quenched due to the large electric field over the QDs, but emission from the cavity modes remains (the inset of Figure 14(b) shows a fit to the two polarization-split fundamental modes of this cavity).

16.4.3 Angle-resolved reflectivity

The final micro-optical technique that we consider is angle-resolved reflectivity (or transmission), where the reflected (transmitted) signal off a sample surface is monitored as a function of angle (Figure 15). In comparison to the methods described thus far, it differs in that it probes the resonant response of the system, and although we do not discuss them in this chapter, we note that micro-absorption measurements follow a procedure similar to what we describe. Angle-resolved reflectivity measurements are particularly well-suited for characterizing the linear optical properties of planar thin films, yielding information about the electromagnetic waves supported upon illumination at an angle from the surface normal (here, illumination refers to the interrogation beam, and not white light imaging). For example, photonic band gap materials such as thin-film distributed Bragg reflector (DBR) stacks (Yariv 2007) or films of self-assembled photonic crystals (Lopez 2002) may be designed to forbid propagating waves for incidence along certain directions, over wavelength ranges called photonic band gaps. Spectral band gap width and position vary with incidence angle, depending on the sample's structure. In such forbidden bands, the reflectance level is substantial and the transmittance is very low. Outside the band gap, the opposite is generally observed, as

propagating waves accessible from outside the structure are available. Tracking band gap position with incidence angle gives insight about the photonic crystal band structure and may help determine physical parameters of the structure (e.g., layer thickness, refractive index, and lattice constants). In spatially inhomogeneous samples, for instance, involving polycrystalline organic films or photonic crystals (Lopez 2002) with micrometer-scale domains, it is important to limit the probed region to dimensions smaller than that of an average sub-domain, to minimize inhomogeneous broadening of spectral features. A similar situation arises when probing fabricated devices with micrometer-scale dimensions.

Many of the considerations in an angle-resolved reflectivity measurement are the same as what has been discussed for micro-PL in Section 16.2. A significant difference is that in the micro-PL setup of Figure 2, we considered normal incidence excitation and collection, whereas we now want to measure the response as a function of angle (non-normal incidence or collection

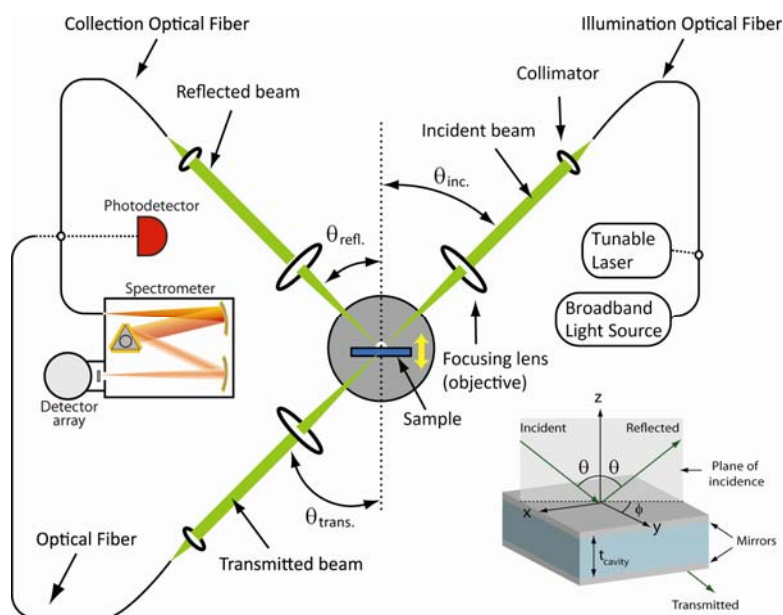


Figure 15: Angle-resolved reflectivity or transmission setup. The goniometer consists of two arms that rotate around a common axis, so that the angle between the two may be precisely adjusted. Collimating and focusing optics, as well as collection and illumination fiber optics shown are mounted on the rotating arms. The bottom right image shows the orientation of the beam on a planar microcavity sample.

may be advantageous in micro-PL characterization of certain sample geometries as well). The main element required is a goniometer, which allows precise control of optical beam incidence and collection angles. The goniometer includes one or more arms that rotate around an axis, and are equipped with optical elements for directing, focusing and collecting optical beams (Figure 15). If a single rotating arm is employed, the sample mount must allow for rotation as well, so all angles may be accessed. Multimode optical fibers are generally employed on movable arms, serving as either excitation or collection ports, and can significantly reduce the complexity of the system. Collimation, focusing, and collection of light from and into the fibers are accomplished as discussed in Sections 16.2.2 and 16.2.3. Short focal lengths generally afford tighter focusing, but low NAs lead to illumination with, and collection of, a smaller angular spread, resulting in improved angular resolution. Objectives are often used as focusing and collection lenses, offering small focal lengths with low NAs , as well as aberration correction (Lopez 2002). The total angular range accessed by the apparatus is limited to a range for which the objectives do not touch the sample or each other, so that long working distance objectives are generally advisable. Additional elements such as polarizers and waveplates may be placed in the collimated beam paths on the arms, to control the incident beam polarization and select the collected beam polarization. The incident beam should meet the sample at the goniometer axis, to prevent the illumination area from moving, and to minimize variations in collected power as the incidence angle is changed. A translation stage adjusts the sample position with respect to the rotation axis and the illuminating beam. If the sample is mounted on a rotating stage, its rotation axis must be aligned with that of the goniometer. If two rotating arms are used, the axes must be coincident.

The light source must have a sufficiently broad spectrum to cover the entire range of the dispersion curves. Common sources are tungsten-halogen incandescent lamps, which provide a

spectrum ranging from visible to near-infrared wavelengths, and Hg(Xe) arc lamps, which provide UV to NIR coverage. Another possibility are fiber supercontinuum sources, which, although pulsed, cover extremely broad wavelength ranges, and provide high power, coherent light beams that are easier to focus. When broadband sources are used, the signal coupled into the collection fiber is brought into a spectrometer, where it is dispersed to reveal the reflectance or transmittance spectra. Alternately, a tunable laser may be used with a photodetector for better spectral resolution, albeit usually at the expense of measurement time and spectral bandwidth.

As an example, we consider measurements of the dispersion characteristics of planar microcavity resonant modes (Lidzey 1995, Kena-Cohen PRL 2008). Such one-dimensional cavities (Figure 15) generally consist of a planar, partial reflector pair sandwiching a sub-wavelength-thickness film of an arbitrary material. The cavity modes are traveling waves in the two planar dimensions (x and y in Figure 15), and form a discrete set in the perpendicular dimension (z). Illumination with a plane wave at an incidence angle θ with respect to the surface normal leads to excitation of a cavity mode with matching parallel wave vector (\mathbf{k}_{\parallel}). For a fixed frequency ω , varying θ allows this condition to be met for all (discrete) cavity mode values. As such, dispersion measurements involve illumination of the cavity at varying θ and spectral analysis of the reflected and/or transmitted light. Cavity resonances are manifested as relatively sharp maxima (minima) in the transmitted (reflected) spectra, in analogy with a Fabry-Perot cavity in which only light of certain frequencies is transmitted. These resonances shift in wavelength as the incidence angle is varied. The dispersion, $\omega(\mathbf{k}_{\parallel})$, is obtained from the position of the resonant maxima or minima at each angle, and is clearly a function of the linear optical properties of the cavity material, expressed through a complex refractive index $n(\omega)$.

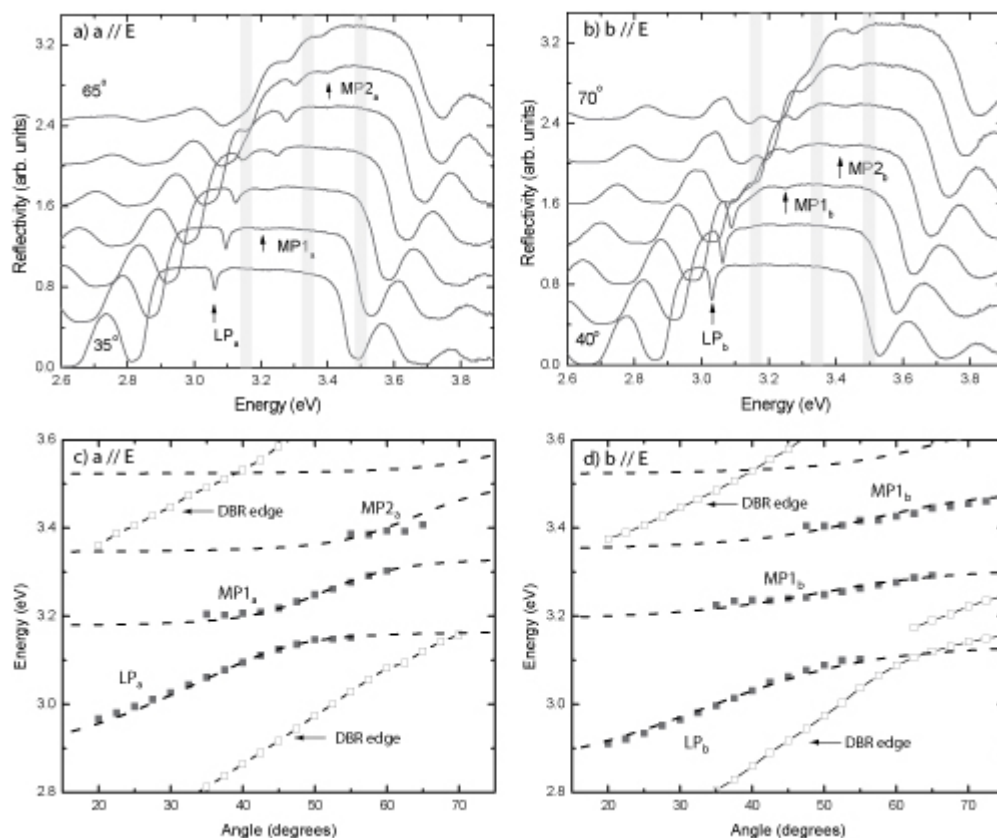


Figure 16: TM (p)-polarization reflection spectra from a 140 nm thick single anthracene crystal cavity with SiN/SiO₂ DBR mirrors, for various incidence angles, and electric field oriented parallel to the monoclinic anthracene crystal **a** (a) and **b** (b) axes. The lower polariton (LP_{a,b}) and middle polariton (MP1,2_{a,b}) branch reflectivity dips are indicated in the figures. Gray boxes indicate the position of bare anthracene film excitonic transitions. The spectral position of the polaritonic dips in (a) and (b) are plotted as a function of angle in (c) and (d), respectively (solid squares). Open squares: DBR stopband edges. Dashed lines: fitted curves using a four-body coupled harmonic oscillator Hamiltonian [Kena-Cohen 2008]. Reprinted with permission from (Kéna-Cohen 2008). Copyright 2008 by the American Physical Society

Figure 16(a)-(b) shows reflectivity spectra for varying incidence angles obtained from a 140 nm thick cavity containing a single anthracene crystal sandwiched between two SiN/SiO₂ DBR mirrors (Kena-Cohen 2008). Due to the fabrication process, the organic microcavity was formed over 500 μm wide, 2 cm long channels, bound by gold stripes. The channel width imposed an upper limit to the illumination spot size, requiring focusing optics to produce spots of diameter <300 μm. As these cavities contain an excitonic material, the dispersion curves show

spectral signatures of strong exciton-cavity photon coupling (Weisbuch 1992). This is evidenced by anti-crossing in the dispersion curves (Figure 16(c)-(d)) traced out from the spectral minima and maxima, and physically represents the formation of normal modes of the two coupled oscillators. By adjusting the polarization of the illumination source, modes in which the electrical field is both parallel and perpendicular to the cavity plane, known respectively as transverse electric (TE) and transverse magnetic (TM) polarization modes (Chapter 1), may be accessed. Such polarization selectivity can be of importance in studying anisotropic materials. Illumination of different spots across the sample revealed variations of tens of meV in the measured polaritonic energies, a result of inhomogeneities in both the crystalline material and cavity parameters. This reinforces the necessity of probing sufficiently small areas to avoid inhomogeneous broadening of reflectivity or transmission spectra.

16.5 Tips when building micro-optical setups

In this final section, we outline a pair of useful procedures when aligning a micro-optical system.

16.5.1 Beam alignment

This section describes the basic process of aligning an optical setup. As a prototypical example, we use the alignment of a collimated beam into a single mode optical fiber, but the process involved is universal for tasks where both the position and slope/angle of an optical beam are important. The setup (Figure 17) consists of a detector, two mirrors (M1 and M2) and kinematic mounts, an optical fiber, an incoupling lens (usually an asphere, microscope objective, or high power achromatic doublet), and a kinematic fiber coupling stage (three or five axis - usually three is sufficient). The first task is to set up the fiber stage by mounting the fiber tip at the manufacturer's specified focus of the incoupling optic (henceforth referred to as the lens). Recall that the optic should be chosen based on the collimated beam diameter, fiber mode field

diameter, and wavelength of light, as discussed in Section 16.2. Then, the fiber position should be fixed in the xy plane so that it is at the center of the lens. For a five-axis stage, the angles should be set so that the axis of the fiber is aligned with the optical axis of the lens. Place M1 so that the collimated beam is centered on it and roughly align it so that the beam is directed onto the center of M2. Then, align M2 so that the beam is centered on the lens, and check to see if the detector is showing at least a very weak signal - if a photodiode is used for detection, it may be necessary to use a high parallel resistance to amplify the measured voltage. If no signal is found, adjust M2 while monitoring the detected signal until power is detected.

The next part of the process is commonly referred to as beam walking. It is a procedure that iteratively aligns the beam to achieve the optimal position (i.e. on the core of the fiber) and slope in the x and y directions, and proceeds as follows: (1) Slightly adjust the x knob of M2, noting the adjustment direction. The signal should be reduced. (2) Adjust the x knob of M1 to optimize the signal and compensate for the signal loss due to the adjustment of M2. If the

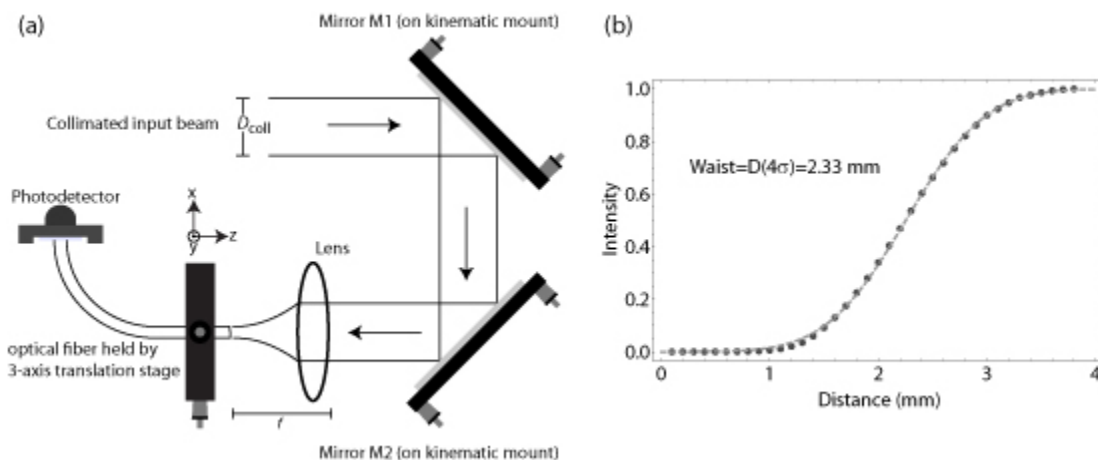


Figure 17: (a) Schematic of a beam alignment setup for coupling a collimated beam into a single mode optical fiber. (b) Measurement of a collimated beam profile using the knife-edge technique.

signal has increased compared to the value before M2's adjustment, then the beam is being walked in the correct direction and M2 should be slightly adjusted in the same manner as before, followed by adjustment of M1. (3) Iterate until the signal reaches a maximum. If the initial

signal is not surpassed by adjustment of M1, then the beam should be walked in the opposite direction. Again, iterate until the signal reaches a maximum and plateaus. If slight adjustments are not resulting in increased signal strength, then use larger adjustments of M2. (4) Once this procedure has been completed for the x direction, do the same for y . (5) After y is finished, redo the procedure for x . Go back and forth between x and y until no more gains in detected power can be made. At this point, the beam is aligned as well as possible for the settings of the lens.

To further optimize the incoupled power, one must adjust the distance between the lens and fiber. Adjust this distance to maximize the detected power, and then adjust M2 and look for a further increase. Continue adjusting the focal distance and M2, and iterate until no more gains are made. At this point, the beam should be optimally aligned. Minor improvement can be made by small adjustments of the x - y position of the lens (or fiber) along with adjustments of M2, but these gains are usually small and come at the cost of using the relatively insensitive actuators of the lens or fiber. While incoupling efficiency depends on the beam quality and optics, typical values should be near 50 %. Efficiency far less than 50 % indicates that a local maximum may have been reached, in which case it is best to start over and make larger initial adjustments of M1 and M2 to better span parameter space. If efficiency remains low, it likely means that a different focusing optic is required or that the collimation/shaping of the input beam needs adjustment.

16.5.2 Beam profiling

The collimated beam size is important because it determines the appropriate lens focal length for coupling into a fiber or a spectrometer. A simple way to measure the transverse extent of a beam is the knife-edge method. The basic principle is to move a sharp metal edge across the beam while measuring the transmitted power. For a Gaussian beam centered at x_0 , the detected power (neglecting diffraction) as a function of knife edge position x_m is

$$P(x_m) = \frac{P_o}{2} \left[1 + \operatorname{Erf} \left(\frac{x_m - x_o}{w/\sqrt{2}} \right) \right], \quad (11)$$

where P_o is the power of the beam when the knife edge does not interfere, $\operatorname{Erf}(x)$ is the error function, defined as $\operatorname{Erf}(x) = \frac{2}{\sqrt{\pi}} \int_0^x e^{-x^2} dx$, and w is the beam waist defined in Section 16.2.2.2.

The setup consists of a razor blade mounted to a micrometer-driven translation stage, along with a broad area detector such as a power meter. Starting the measurement with the razor blade completely blocking the beam sets the background level, and the power is then noted as a function of blade position. For a Gaussian beam, the background-subtracted data should look similar to that in Figure 16(b), which can then be fit to equation 11 to determine the beam waist.

Acknowledgements

We thank colleagues with whom we have built the characterization setups that informed the presentation in this chapter, including Oskar Painter, Paul Barclay, Stefan Strauf, and Stephane Kéna-Cohen. We also thank Antonio Badolato, our collaborator on near-infrared quantum dot studies, and Andrew Berglund for helpful comments on the chapter. Portions of the work described were performed at the NIST Center for Nanoscale Science and Technology, and partly supported by the NIST-CNST/UMD-NanoCenter Cooperative Agreement.

References

- [Aspect 1980] Aspect, A., Roger, G., Reynaud, S., Dalibard, J., and Cohen-Tannoudji, C. 1980. Time correlations between the two sidebands of the resonance fluorescence triplet. *Physical Review Letters* 45: 617-620.
- [Alivisatos 1996] Alivisatos, A.P. 1996. Semiconductor clusters, nanocrystals, and quantum dots. *Science* 271: 933-937

- [Badolato 2008] Badolato, A., Winger, M., Hennesy, K.J., Hu, E.L., and Imamoglu, A. 2008. Cavity QED effects with single quantum dots. *Comptes Rendus Physique* 9: 850-856.
- [Balistreri 1999] Balistreri, M.L.M., Klunder, D.J.W., Blom, F.C. et al. 1999. Visualizing the whispering gallery modes in a cylindrical optical microcavity. *Optics Letters* 24: 1829-1831.
- [Basche 1992] Basche, Th., Moerner, W.E., Orrit, M., and Talon, H. 1992. Photon antibunching in the fluorescence of a single dye molecule trapped in a solid. *Physical Review Letters* 69: 1516-1519.
- [Bayer 2002] Bayer, M. and Forchel, A. 2002. Temperature dependence of the exciton homogenous linewidth in $\text{In}_{0.60}\text{Ga}_{0.40}\text{As}/\text{GaAs}$ self-assembled quantum dots. *Physical Review B* 65: 041308.
- [Becker 2005] Wolfgang Becker. 2005. *Advanced Time-Correlated Single Photon Counting Techniques*. Berlin: Springer
- [Betzig 1993] Betzig, E. and Chichester, R.J.. 1993. Single molecules observed by near-field scanning optical microscopy. *Science* 262: 1422-1425.
- [Coldren 1995] Coldren, Larry A. and Scott W. Corzine. 1995. *Diode Lasers and Photonic Integrated Circuits*. New York: John Wiley & Sons
- [Delhaye 1975] Delhaye, M. and P. Dhamelincourt. 1975. Raman microprobe and microscope with laser excitation. *Journal of Raman Spectroscopy* 3: 33-43.
- [Demtroder 1998] Demtroder, Wolfgang. 1998. *Laser Spectroscopy*. Berlin: Springer-Verlag.
- [Diels 2006] Diels, Jean-Claude and Wolfgang Rudolph. 2006. *Ultrashort Laser Pulse Phenomena*. Amsterdam: Elsevier (Academic Press)
- [Drexler 1994] Drexler, H., Leonard, D., Hansen, W., Kotthaus, J.P., and Petroff, P.M. 1994. Spectroscopy of Quantum Levels in Charge-Tunable InGaAs Quantum Dots. *Physical Review*

Letters 73: 2252-2255.

[Gerardot 2007] Gerardot, B.D., Seidl, S., Dalgarno, P.A. et al. 2007. Contrast in transmission spectroscopy of a single quantum dot. *Applied Physics Letters* 90: 221106.

[Grilli 1992] Grilli, E., Guzzi, M., Zamboni, R., and Pavesi, L. 1992. High-precision determination of the temperature dependence of the fundamental energy gap in gallium arsenide. *Physical Review B* 45: 1638-1644.

[Gruber 1997] Gruber, A., Drabenstedt, A., Tietz, C., Fleury, L., Wrachtrup, J., and von Borczyskowski, C. 1997. Scanning confocal optical microscopy and magnetic resonance on single defect centers. *Science* 275: 2012-2014

[Gustafsson 1998] Gustafsson, A. 1998. Local probe techniques for luminescence studies of low-dimensional semiconductor structures. *Journal of Applied Physics* 84: 1715-1775.

[Hecht 1998] Hecht, Eugene. 1998. *Optics*. Reading: Addison-Wesley

[Hell 2009] Hell, S.W. 2009. Microscopy and its focal switch. *Nature Methods* 6:24-32

[Hobbs 2000] Hobbs, Philip C.D. 2000. *Building Electro-Optical Systems: Making it All Work*. New York: John Wiley & Sons

[Kasai 1995] Kasai, J. and Katayama, Y. 1995. Low-temperature micro-photoluminescence using confocal microscopy. *Review of Scientific Instruments* 66: 3738-3743.

[Kena-Cohen 2008] Kéna-Cohen, S., Davanço, M., and Forrest, S. R. 2008. Strong Exciton-Photon Coupling in an Organic Single Crystal Microcavity. *Physical Review Letters* 101: 116401

[Kimble 1977] Kimble, H.J., Dagenais, M., and Mandel, L. 1977. Photon antibunching in resonance fluorescence. *Physical Review Letters* 39: 691-695.

[Krauss 2009] Krauss, G., Lohss, S., Hanke, T., et al. 2009. Synthesis of a single cycle of light with compact erbium-doped fibre technology. *Nature Photonics* 4:33-36.

[Kurtsiefer 2000] Kurtsiefer, C., Mayer, S., Zarda, P., and Weinfurter, H. 2000. Stable solid-state of single photons. *Physical Review Letters* 85: 290-293.

[Levi 1992] Levi, A.F.J., Slusher, R.E., McCall, S.L., Tanbun-Ek, T., Coblentz, D.L., and Pearton, S.J. 1992. Room temperature operation of microdisk lasers with submilliamp threshold current. *Electronics Letters* 28: 1010-1012.

[Lidzey 1995] Lidzey, D. G. , Bradley, D. D. C. , Skolnick , M. S. , Virgili, T., Walker ,S. and Whittaker, D.M., 1995. Strong exciton–photon coupling in an organic semiconductor microcavity, *Nature* 395: 53-55.

[Lopez 2002] Lòpez, J. F. G., and Vos, W. L. 2002. Angle-resolved reflectivity of single-domain photonic crystals: Effects of disorder. *Physical Review E* 66: 036616.

[Mandel 1995] Mandel, Leonard and Emil Wolf. 1995. *Optical coherence and quantum optics*. Cambridge: Cambridge University Press.

[McCall 1992] McCall, S.L., Levi, A.F.J., Slusher, R.E., Pearton, S.J., and Logan, R.A. 1992. Whispering-gallery mode lasers. *Applied Physics Letters* 60:289-291

[Michler 2000] Michler, P., Imamoglu, A., Mason, M.D., et al. 2000. Quantum correlation among photons from a single quantum dot at room temperature. *Nature* 406: 968-970.

[Michler 2003] Michler, Peter. 2003. *Single quantum dots*. Berlin: Springer-Verlag

[Murray 1993] Murray, C.B., Norris, D.J., and Bawendi, M.G. 1993. Synthesis and characterization of nearly monodisperse CdE (E=S, SE, TE) semiconductor nanocrystallites. *Journal of the American Chemical Society* 115: 8706-8715

[Moerner 1999] Moerner, W.E., and Orrit, M. 1999. Illuminating single molecules in condensed matter. *Science* 283: 1670-1676

[Moerner 2003] Moerner, W.E. and Fromm, D.P. 2003. Methods of single-molecule

fluorescence spectroscopy and microscopy. *Review of Scientific Instruments* 74: 3597-3619.

[Moreau 2001] Moreau, E., Robert, I., Manin, L., Thierry-Mieg, V., Gerard, J.-M., and Abram, I. 2001. Quantum cascade of photons in semiconductor quantum dots. *Physical Review Letters* 87: 183601.

[Novotny 2006] Novotny, Lucas and Bert Hecht. 2006. *Principles of Nano-Optics*. Cambridge: Cambridge University Press

[Paschotta 2008] Rudiger Paschotta. 2008. *Encyclopedia of Laser Physics and Technology*. Berlin: Wiley-VCH

[Rakher 2008] Matthew T. Rakher. 2008. *Quantum optics with quantum dots in microcavities*. PhD thesis, University of California, Santa Barbara.

[Ribordy 1998] Ribordy, G., Gautier, J.-D., Zbinden, H. and Gisin, N. 1998. Performance of InGaAs/InP avalanche photodiodes as gated-mode photon counters. *Applied Optics* 37: 2272-2277.

[Robbins 2003] Robbins, M.S. and Hadwen, B.J. 2003 The noise performance of electron multiplying charge coupled devices. *IEEE Transactions on Electron Devices* 50: 1227-1232

[Santori 2002] Santori, C., Fattal, D., Vuckovic, J., Solomon, G.S., and Yamamoto, Y. 2002. Indistinguishable photons from a single-photon device. *Nature* 419: 594-597.

[Santori 2004] Santori, C., Fattal, D., Vuckovic, J., Solomon, G.S., Waks, E., and Yamamoto, Y. 2004. Submicrosecond correlations in photoluminescence from InAs quantum dots. *Physical Review B* 69: 205324.

[Siegman 1986] Anthony Siegman. 1986. *Lasers*. Sausalito: University Science Books

[Srinivasan 2003] Srinivasan, K., Barclay, P.E., Painter, O., Chen, J., Cho, A.Y., and Gmachl, C. 2003. Experimental demonstration of a high-Q photonic crystal microcavity. *Applied Physics*

Letters 83: 1915-1917.

[Srinivasan 2007] Srinivasan, K., Painter, O., Stintz, A., and Krishna, S. 2007. Single quantum dot spectroscopy using a fiber taper waveguide near-field optic. *Applied Physics Letters* 91: 091102.

[Strauf 2006] Strauf, S., Hennessy, K., Rakher, M.T., et al. 2006. Self-tuned quantum dot gain in photonic crystal lasers. *Physical Review Letters* 96: 127404.

[Vurgaftman 2001] Vurgaftman, I., Meyer, J.R., and Ram-Mohan, L.R. 2001. Band parameters for III-V compound semiconductors and their alloys. *Journal of Applied Physics* 89: 5815-5875.

[Weisbuch 1992] Weisbuch, C., Nishioka, M., Ishikawa, A., and Arakawa, Y. 1992. Observation of the coupled exciton-photon mode splitting in a semiconductor quantum microcavity. *Physical Review Letters*.69: 3314-3317.

[Yariv 2007] Yariv, Amnon and Pochi Yeh. 2007. *Photonics: Optical Electronic in Modern Communications*. New York: Oxford University Press

[Yuan 2002] Yuan, Z.L., Kardynal, B.E., Stevenson, R.M., et al. 2002. Electrically driven single-photon source. *Science* 295: 102-105.